2

Inertia friction welding (IFW) for aerospace applications

M. M. ATTALLAH, University of Birmingham, UK and
M. PREUSS, University of Manchester, UK

Abstract: The use of inertia welding in the aerospace industry has been steadily increasing owing to the significant improvements it provides in joint quality, compared with the use of fusion welding. This chapter introduces the process, with respect to its operation, parameters, differences from other friction welding techniques and equipment. It also explains the application of the technique and the selection of the process parameters, and the different mathematical, analytical and numerical approaches that are used to model the thermal fields and residual stress development. Details of the microstructural, mechanical properties and residual stress development in inertia friction-welded Ni-based superalloys, titanium alloys, steels and other alloys are also discussed.

Key words: inertia friction welding, nickel superalloys, titanium alloys, steel, finite element modelling, microstructure, residual stresses.

2.1 Introduction

The need for high-quality joints, combined with the inherent difficulty in welding most aerospace materials, has fostered the use of solid-state friction-based welding techniques within the past decade in the aerospace industry, such as: friction stir welding (FSW), linear friction welding and rotary friction welding (RFW) with its two variants; continuous-drive friction welding (CDFW) and inertia friction welding (IFW) (Kallee *et al.*, 2003). Except for FSW, friction-based welding processes can be described as self-cleaning as a result of the ejection of the plasticised material in the form of flash at the end of the welding cycle, which carries alongside any surface contamination or oxides, making it unnecessary to use shielding gas during welding. Among the friction-based welding processes, the use of inertia welding in the aerospace industry has been steadily increased in the past two decades, especially in joining nickel-based superalloys, titanium alloys and steel aero engine cylindrical components, owing to the significant improvements it provides in the joint quality, compared with the use of fusion welding. This chapter contains six themes. The first theme introduces the process, with respect to its operation, parameters, differences from other friction welding

techniques and equipment. The second theme explains the application of the technique and the selection of the process parameters, and the different mathematical, analytical and numerical approaches that are used to model the thermal fields and residual stress development. The third and fourth themes discuss the microstructural and mechanical property development respectively, in inertia friction-welded Ni-based superalloys, titanium alloys, steels and other alloys. The impact of the process on the residual stress development is discussed in the fifth theme, focusing on the application of neutron and synchrotron X-ray diffraction in measuring the residual stress development. Finally, the chapter is concluded with a section outlining the future trends and possible developments in IFW.

2.1.1 Process development

Although it is believed that the interest in using rotary frictional heating for joining dates back to a late nineteenth-century U.S. patent, further developments in the first half of the twentieth century resulted in the development of commercially applicable RFW techniques (Oberle *et al.*, 1967). Concurrent yet separate efforts by Russian and American engineers resulted in the development of the two variants of RFW in the second half of the twentieth century. Around 1954–1957, Russian engineers Chudikov and Vill were first to suggest an RFW technique for joining cylindrical sections mounted on a modified lathe, which was later termed direct or continuous-drive friction welding (Chudikov, 1956; Houldcroft, 1977). Upon successful commercialisation of this technique in Russia, the concept of RFW became familiar with American and British engineers. Pioneering work at the Caterpillar Tractor Company led to the development of inertia (flywheel) friction welding (IFW), which was U.S. patented in 1965 (Houldcroft, 1977; Oberle, 1968; Oberle *et al.*, 1967). Because of this, IFW remains more commonly used in the USA until today, while CDFW is mostly used in Europe and Japan.

2.1.2 Inertia friction welding (IFW) process description

In IFW, the kinetic energy stored in a rotating flywheel is conserved into frictional thermal energy to mostly join two components of cylindrical geometry; one component is clamped to the flywheel, while the other component is clamped in a non-rotating chuck connected to a hydraulic ram. During welding, once the flywheel is brought to a certain rotation speed, the motor is disengaged, and a forging pressure is applied to the hydraulic ram to bring the two components to contact. Following the initial contact, the flywheel speed starts to decelerate owing to the conservation of the stored

energy into thermal energy, causing the temperature to increase sharply at the interface owing to the generated friction. Ultimately, a plasticised layer forms between the two components, where consolidation occurs. The application of pressure causes the plasticised material to flow outside the joint line forming a flash, which dissipates some of the weld energy causing the interface region to cool slightly even before the rotating part has come to a halt (Anon, 1979; Oberle *et al.*, 1967).

IFW thus differs from CDFW in the braking mechanism. In CDFW, braking is performed by declutching the spindle from the hydraulic or electric motor that 'continuously' drives the rotating component, followed by applying the brakes upon the application of the forging force for a certain time (Anon, 1979). In IFW, braking occurs upon the dissipation of the energy stored in the flywheel, which occurs gradually during IFW, with the maximum energy transfer occurring upon the first touch between the two interfaces (Kallee *et al.*, 2003). This difference affects the application of the power input to the weld throughout the process; where the power input in IFW changes to supply the required power to first plasticise the interface and then to forge the components, while the power input in CDFW is limited by the power rating of the motor. The main differences between the IFW and CDFW systems are shown in Fig. 2.1.

2.1.3 IFW process parameters

Both IFW and CDFW processes differ in the parameters that control the process (Anon, 1979). IFW is controlled by two main parameters, which are

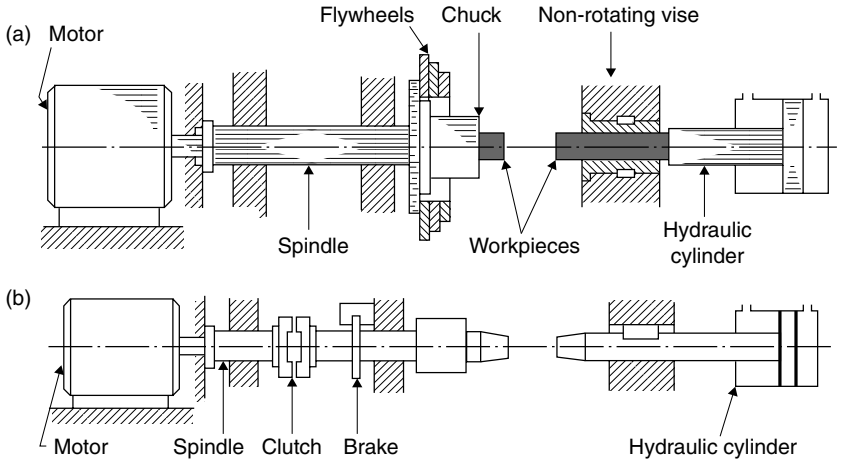

2.1 Schematic diagrams for the set-ups of the welding systems for (a) inertia welding and (b) CDFW (Anon, 1979).

the welding energy (rotation speed and flywheel inertia) and the forging pressure, while CDFW is controlled by the rotation speed and the time-pressure cycle to be used, including the braking time (Fig. 2.2). It is important to mention that the spindle speed (and hence the power input) gradually decreases from the maximum (set) value following contact in IFW, whereas the spindle speed is mostly constant in CDFW (Houldcroft, 1977). For further details on CDFW (e.g. process parameters, machine specifications and applications), the reader is directed to other references that fully discuss CDFW (Anon, 1979; Ellis, 1972; Hollander *et al.*, 1964).

2.1.4 IFW process stages

A three-stage model is generally used to define the IFW stages depending on the fluctuation in the frictional torque owing to the contact between the rotating components (Wang and Lin, 1974), or four stages if an initial stage is added during which the flywheel reaches the desired rotation speed

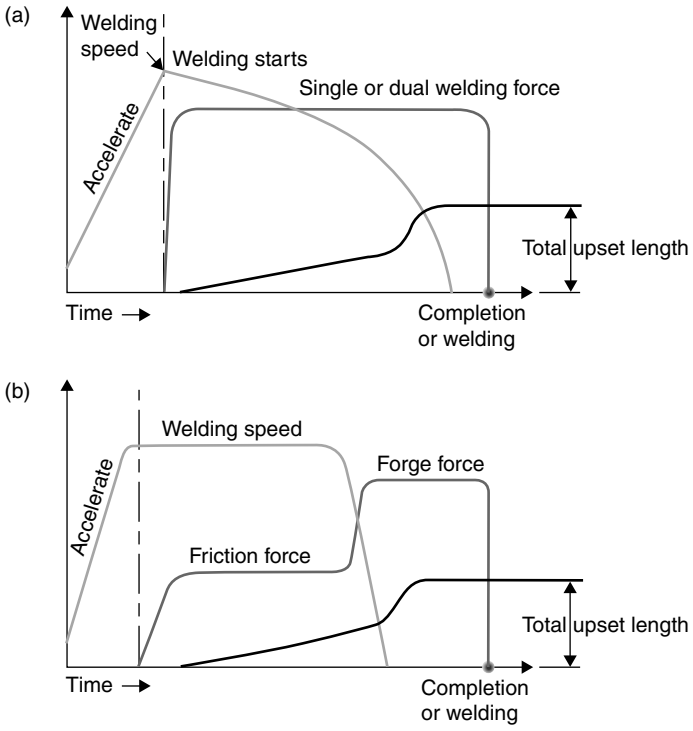

2.2 A comparison between the welding cycle for (a) inertia welding and (b) CDFW. (Courtesy of Manufacturing Technology, Inc.)

(D'Alvise *et al.*, 2002). According to the three-stage model (Fig. 2.3), the three stages are described as follows:

- Stage I (*initial contact*): the two components are brought in contact, which results in a rapid increase in the frictional torque, a deceleration in the rotation speed and accordingly a sizeable dissipation of the stored energy owing to the dry friction between the interfaces. The friction also leads to the removal of any surface irregularities and asperities, similar to what happens during wear, until perfect contact is reached. With the increase in temperature, a decrease in the torque occurs at the end of this stage, owing to the softening of the material and adhesion of asperities at the interface, forming a plasticised layer (Fig. 2.4a). The high torque that is experienced and the high rotation speed at start mean that the maximum power input is achieved within this stage.
- Stage II (*transition stage*): the friction-induced thermomechanical deformation makes the material at the thin interface fully plasticised (visco-plastic). Thus, the process reaches a transitional steady-state condition, where the strain hardening is overcome by frictional heating. This is manifested in a roughly constant torque, and a gradually decreasing

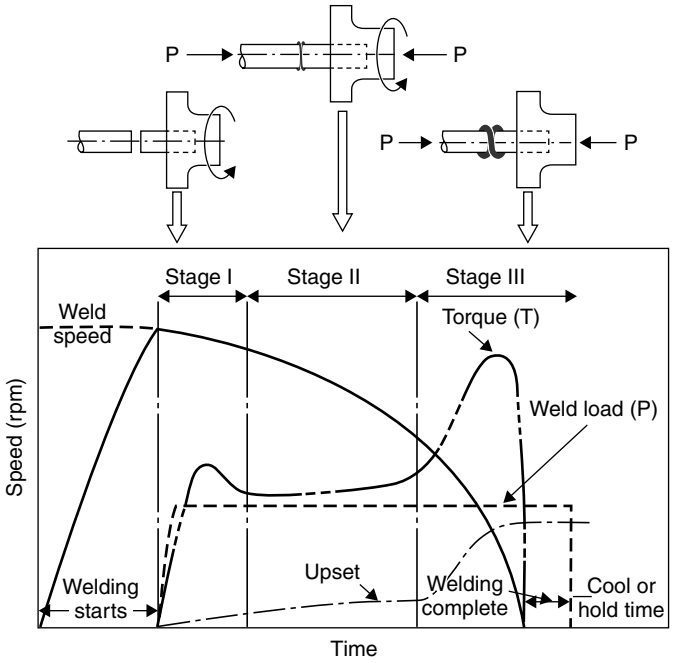

2.3 The stages of inertia welding, showing the variation in process variables (Anon, 1979; Wang and Lin, 1974).

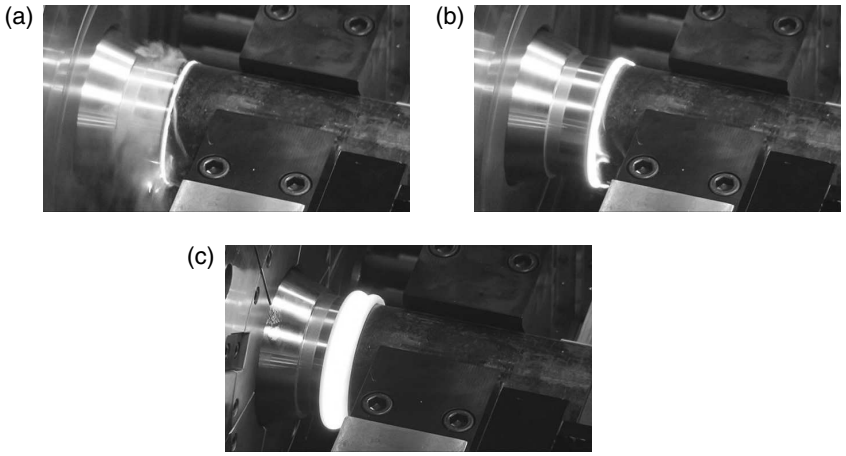

2.4 The stages of inertia welding in a drill-pipe weld (a) initial contact, (b) transitional stage and (c) forging. (Courtesy of Manufacturing Technology, Inc.)

rotation speed (and power). A gradual increase in the upset also occurs owing to burn-off and the initiation of flash formation at the interface. However, continuous frictional heating leads to the widening of the plasticised region (Fig. 2.4b).

- Stage III (*forging stage*): with the decrease in rotation speed while the forging pressure is still being applied, the torque increases to another peak to overcome the cooling and hardening. This increase in torque is believed to refine the joint microstructure at this final stage, as well as the ejection of the flash that carries along any oxides or inclusions (Oberle *et al.*, 1967). The upset increases and more flash is formed, leading to further cooling of the interface (Fig. 2.4c). After reaching the maximum upset, the forging load is kept applied until the weld cools.

2.1.5 IFW production machines

IFW machines are generally classified according to the forge force capacity, which ranges from a fraction of a ton to 4500 ton lb (~8896 kN). The choice of the machine depends on the application geometry and material, which accordingly controls the required process parameters. Typical machines and products are shown in Figs. 2.5 and 2.6. For relatively small aerospace components (e.g. pistons, pipes, turbine wheels and shafts), machines with forging force capacity ~1–50 ton lb (~2–250 kN) are normally used (Fig. 2.5). For larger aero engine assemblies (e.g. compressor-rotor, disk-to-cone, drum-drive compressor and disk-to-shaft assemblies), machines with large capacities are used to provide the required energy (MTI, 2009) (Fig. 2.6).

(a)

(b)

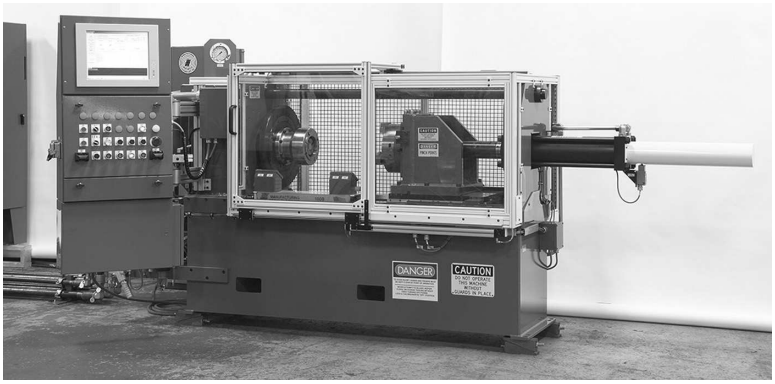

2.5 Typical IFW machines and products (a) 15 ton welder, (b) 40 ton welder, (c) light-weight piston for aircraft pump produced by the 15 ton welder and (d) turbine wheels produced by the 40 ton welder. (Courtesy of Manufacturing Technology, Inc.)

Major suppliers of IFW machines include Manufacturing Technology Inc. (MTI), Blacks equipment, Thompson friction welding, Swanson industries, AI Welders, Kuka and the Welding Institute (TWI). Most IFW machines are horizontal and driven with hydraulic systems, although there are some machines (mostly with small forging force capacity) that run with DC or AC motors (Anon, 1979). In the hydraulic-driven machines, the spindle-flywheel assembly is operated using a hydraulic pump. The pump itself is operated with an electric motor, which switches off once the desired rotation speed

(c)

(d)

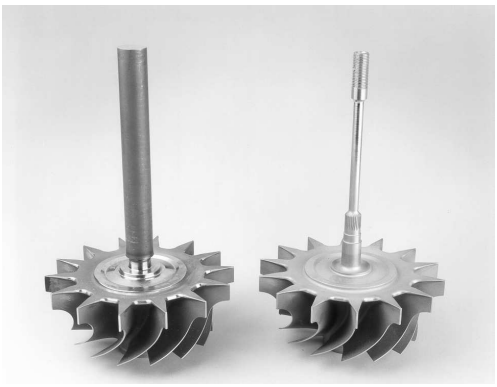

2.5 Continued

is reached. In the electric motor-driven machines, the motor is directly connected to the spindle, and is either declutched or switched off when the required speed is reached.

2.1.6 Advantages and disadvantages of IFW

The use of IFW provides several advantages, either from a manufacturing viewpoint or with respect to the weld structural integrity. Compared with fusion welding, the process is fully automated and repeatable, and does not require the use of a filler material, shielding gases or vacuum owing to its self-cleaning mechanism (i.e. flash formation) (Kallee *et al*., 2003). The process control and optimisation is also simple as it is controlled by only two variables (weld energy and forging pressure) (Anon, 1979), or three variables if the weld energy is separated into the flywheel inertia and rotation speed. Similar, dissimilar and components of different geometries

(a)

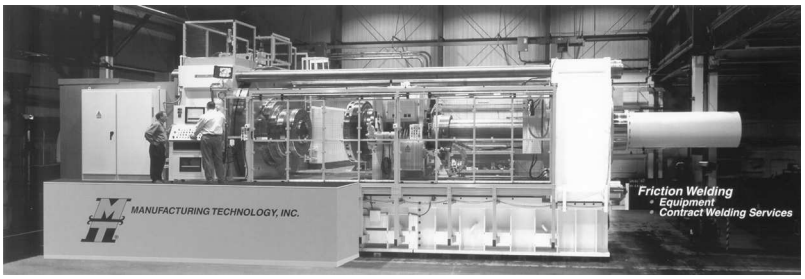

(b)

2.6 (a) A 2000 ton forge force inertia welder (model 2000B) and (b) a titanium low-pressure rotor assembly for an aero engine produced using the 2000 ton welder. (Courtesy of Manufacturing Technology, Inc.)

are also weldable using IFW. In addition, the process results in a more efficient material utilisation, weight reduction and a longer component life compared with using bolted joints (Heberling, 1990). Moreover, the solid-state nature means that any solidification defects are avoided. The joint possesses several unique characteristics, with respect to its microstructure and mechanical properties, as will be discussed later. Finally, IFW is a safe and environmentally friendly technique as it does not produce any harmful gases, fumes, etc.

Nonetheless, IFW requires a remarkable capital investment in the machinery and tooling, although the capability of the IFW machine can be tailored according to the geometry of the application required (Benn, 2000). Still, the introduction of new applications can be expensive and requires a long lead time. In addition, there is a shortage in qualified welders as it is a very specialised process. Thus, if only a limited number of IFW joints are required, acquiring an IFW machine might not be economically sustainable.

2.2 Process parameters, heat generation and modelling

2.2.1 Process parameters and joint design

The selection of the welding parameters in IFW is dependent upon the component material and geometry, which is then used to determine the required welding energy. Manufacturers of IFW machines have typically produced charts that determine the required energy based on the section diameter for solid cylinders, or the wall thickness for tubular sections. Owing to the origin of IFW being in the USA, most IFW variables, parametric tables and charts are available in imperial units, although modern inertia welders follow the metric system.

The stored energy (E, lb/ft^2) in the flywheel of inertia (Wk^2, lb/ft^2) and rotation speed (N, rpm) is given as:

$$\frac{E = (Wk^2 \times N^2)}{5873} \quad [2.1a]$$

In SI units, the above equation becomes:

$$E = \frac{I \times N^2}{182.38} \quad [2.1b]$$

where I is the inertia (kg.m^2).

The linear speed of the outer diameter is presented as surface feet per minute (s.f.p.m.), which is calculated using:

$$\text{s.f.p.m.} = 2\pi N \times r \quad [2.2]$$

where r is the outer radius in feet.

It is usually required to calculate the energy per unit area (E/A) and load applied per unit area (L/A), which is performed by dividing over the contact area. The following example illustrates the methods for the calculation of the IFW process parameters. The material data and parameters are based on the information supplied in the manual of the M120 inertia welder, Manufacturing Technology Inc. (MTI, 1974).

Example

Most machine manuals include charts similar to the one shown in Fig. 2.7, which can be used to determine the energy and load required for welding tubular sections or bars of mild steel. For any material other than mild steel and any geometry other than bar-to-bar or tube-to-tube, material

factors (e.g. for Al, Ti, Ni alloys) and geometry factors (e.g. bar-to-tubes, bar-to-plate, tube-to-plate, etc.) are used to calculate the required energy and load, whereby:

$$E = \text{energy for mild steel} \times \text{material factor} \times \text{geometry factor} \quad [2.3a]$$

$$L = \text{load for mild steel} \times \text{material factor} \times \text{geometry factor} \quad [2.3b]$$

To weld a 3/4 inch (19.05 mm) mild-steel bar, a weld energy of $E = 15\,000$ ft.lbs (20.3 kJ) and a load of $L = 7250$ lbs (32.25 kN) are required. For the same alloy, a speed (s.f.p.m.) range of ~1200–1800 ft/min (365–548 m/min) can be possibly used. As the used chart was for bars of mild steel, both the material and geometry factors are reduced to unity.

To calculate the inertia and rotation speed required based on the energy required, machine manufacturers suggest two approaches. In the first approach, an average value of the typical rotation-speed range to weld a specific material is used to calculate the inertia required using Equation [2.1]. As the flywheels available for each machine have specific inertias that most likely do not match the theoretical inertia, the nearest flywheel assembly is used. Finally, the rotation speed is recalculated based on the inertia of the available flywheel. It is important to point out that the energy is more sensitive to changes in the rotation speed than the inertia (Equation [2.1]). In the second approach, a chart for the total energy plotted against the spindle speed is used for each of the flywheels or flywheel combinations available as shown in Fig. 2.8. This approach eliminates the need to recalculate the rotation speed.

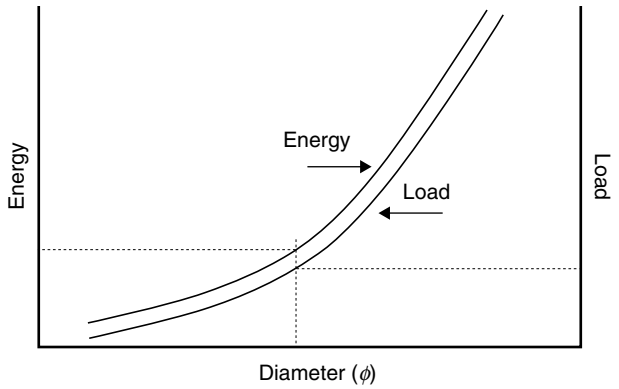

2.7 A typical 'process-parameters' determination chart.

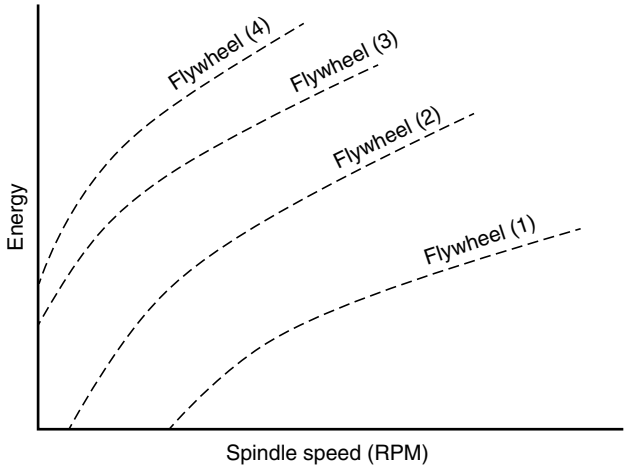

2.8 An alternative chart for the determination of the rotation speed and inertia.

To ensure reliable forging between the two parts, machines are equipped with displacement transducers to control the amount of upset, as a minimum upset is required to ensure that any inclusions or oxides are fully ejected out of the weld in the form of flash. The following formulae give an approximate estimate for the target upset to yield an acceptable weld (Benn, 2000):

$$\text{Target upset} = 0.15\text{”} (3.81 \text{ mm}) + 0.2 \times \text{tube thickness} \quad [2.4a]$$

$$= 0.05\text{”} (1.27 \text{ mm}) + 0.2 \times \text{bar diameter} \quad [2.4b]$$

Knowing that there is a reasonable range of welding parameters that can be used for different materials, the increase in a certain parameter can change the extent of upset and the morphology of the welding region. Upon increasing the flywheel energy, the amount of flash and upset are known to increase. For the peripheral speed, the morphology of the weld region develops from being concave to convex on increasing the speed, with the weld performed at low speed having poor quality at the centre. This is also the case with the welds performed with a high forging pressure (Elmer and Kautz, 1993).

2.2.2 Heat generation

An important issue in modelling friction welding is the mathematical representation for heat generation. Early analytical models utilised the actual power measured by the welding machine after subtracting the idle power

(Cheng, 1962), until Cheng (1963) suggested that the power input can be described using the instantaneous measured value of the torque (M_t) and rotation speed (N_t) such that:

$$q = \frac{2\pi}{K} M_t N_t \qquad [2.5]$$

where q is the power input, and K is a constant.

On modelling IFW, Wang and Nagappan (1970) suggested a friction-induced heat-generation model, where the power input at a certain radial position, r, can be represented by:

$$q = K_I \mu p r N_t \qquad [2.6]$$

where K_I is a constant, μ is the coefficient of friction, and p is the forging pressure. The total heat generation for an annular element or thickness dr can be represented as:

$$Q = K_{II} \int_0^T \int_0^R \mu(r,t) \cdot p(r,t) \cdot N_t \cdot r^2 \cdot dr \cdot dt \qquad [2.7]$$

where K_{II} is a constant. The friction coefficient was also suggested to be varying with position and time as given by:

$$\mu(r,t) = \frac{K}{(N_t r)^2} \qquad [2.8]$$

This formulation, although analytically correct, results in a complicated computation to estimate the heat input. Thus, it was suggested that the product μp is constant throughout the welding process, which is calculated from the average value of the heat generation. Equation [2.7] can be integrated after substituting N_t with a second-order polynomial function for the variation of N with time.

It is apparent that the spatial variation in the friction coefficient, as well as with temperature, resulted in making the measured power-input-based approaches more popular than the friction-based approach. Other power-input (Johnson *et al.*, 1966) models were suggested for IFW, where the actual power input was modelled in two functions (stages). The first stage represents the initial contact stage, followed by the decrease in power in the second stage, as shown in Fig. 2.9:

$$\text{Stage I}: q_I = q_{\max} \sin \omega t \qquad [2.9a]$$

$$\text{Stage II}: q(t) = \left(\frac{k\rho c}{\pi}\right)^{1/2} T_S t^{-1/2} \qquad [2.9b]$$

where q_{max} is the maximum power input, T_s is the maximum interface temperature, c is the specific heat, ρ is the density, t is time and k is the thermal conductivity. A review of other models that rely on the measured power input is available elsewhere (Davé *et al.*, 2001).

2.2.3 Analytical and numerical (finite-difference) modelling

Early IFW modelling efforts focused on developing thermal analytical models, prior to the wider application of the finite element method for thermal and thermomechanical modelling in recent years. A review of the early analytical models for friction welding, which were mostly generated in the former Soviet Union, is available elsewhere (Davé *et al.*, 2001). These models rely on obtaining closed-form solutions for the two-dimensional heat-transfer differential equation:

$$\frac{\partial^2 T}{\partial r^2} + \frac{1}{r}\frac{\partial T}{\partial r} + \frac{\partial^2 T}{\partial z^2} = \frac{1}{\alpha}\frac{\partial T}{\partial t} \qquad [2.10]$$

This approach uses some assumptions to simplify obtaining the mathematical solution (e.g. assuming a semi-infinite solid, constant thermophysical

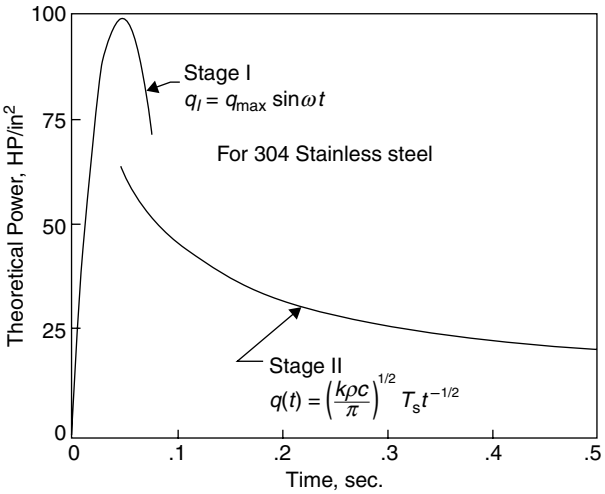

2.9 Power-input-based modelling for inertia welding according to Johnson *et al.* model (Wang and Lin, 1974).

properties and constant heat flux). The resulting solutions are given by equations in the form of:

$$T = \left(\frac{2q_O}{k}\right) \cdot \sqrt{\alpha t} \cdot ierfc\left(\frac{x}{2\sqrt{\alpha t}}\right); 0 \le t \le t_h \quad [2.11]$$

where T is the temperature, q_O is the surface heat flux, k is the thermal conductivity, α is the thermal diffusivity, x is the distance from the weld line, t is the time and t_h is the total time for the heat-flux application. It is not clear though how the heat flux is calculated based on the welding parameters. Further details on this approach can also be found elsewhere (Grong, 1997).

Later, Cheng was the first to develop numerical (finite-difference) solutions for a one-dimensional heat-transfer equation, including in the model a melt (moving) boundary at the interface (Cheng, 1962, 1963). The calculated thermal fields were compared with thermocouple measurements during CDFW that showed that the model underestimated the temperatures in the initial heating phase, prior to decreasing the under-shoot by the end of the heating cycle. Cheng also investigated the influence of using variable and constant thermophysical properties (Cheng, 1962), and compared the numerical results with the heat-balance (closed-form) integral method. The concept of the melting interface was later disproved by performing thermocouple measurements across a mild-steel inertia friction weld (Wang and Nagappan, 1970) and using analytical flow modelling (Davé *et al.*, 2001). This also becomes clearer by investigating the weld microstructure as will be discussed later. Most of the aforementioned modelling attempts were mainly for CDFW, which was the more familiar RFW process in the 1960s. Thus, it was not until the 1970s when Cheng's numerical approach was applied to model IFW (Wang and Lin, 1974; Wang and Nagappan, 1970). A two-dimensional numerical formulation was used, with temperature-dependent thermophysical properties. Nonetheless, the models also showed a deviation from the thermocouple measurements, which was more noticeable towards the centre of the welded section.

2.2.4 Thermal and thermomechanical modelling

With the advance in using the finite-element (FE) method, several models were developed to model the thermal fields (Bennett *et al.*, 2007; D'Alvise *et al.*, 2002; Jeong *et al.*, 2007; Fu *et al.*, 2003; Grant *et al.*, 2009; Liwen *et al.*, 2004; Moal and Massoni, 1995; Soucail *et al.*, 1992; Wang *et al.*, 2005), deformation stresses (D'Alvise *et al.*, 2002; Fu *et al.*, 2003; Moal and Massoni, 1995; Soucail *et al.*, 1992) and residual stress development (Bennett *et al.*, 2007; D'Alvise *et al.*, 2002; Grant *et al.*, 2009; Wang *et al.*, 2004, 2005). The main

factor in assessing the quality of an FE model is the performance of the validation using the measured process variables (e.g. welding time, temperatures, upset and weld (flash) morphology), as well as the weld properties (e.g. microstructural development and residual stresses). Nonetheless, early models did not sufficiently characterise the microstructure or the residual stress characterisation.

Among the early models, Moal and co-workers established a two-dimensional FE code (INWELD) to model the thermal and strain-field development, owing to IFW in the Astroloy powder metallurgy Ni-based superalloy (Moal and Massoni, 1995; Soucail *et al*., 1992). Their model was complemented with in-depth mechanical (torsion) testing and microstructural characterisation to model the high-temperature deformation, dissolution/precipitation and rapid-heating kinetics of the γ' dissolution process (Soucail *et al*., 1992). The mechanical characterisation was used to construct the rheological thermomechanical constitutive equations for the material using Norton-Hoff law. The microstructural studies were used to predict the thermal fields owing to IFW based on the γ' precipitates development, which suggested that the temperature at the weld centre approached ~1280°C (above the γ' solvus but well below melting temperature). The heat generation in the model was friction-induced using Coulomb's friction law developing to viscous flow at high temperatures. This required the calculation of the rotational velocity at each step, with the temperature and stress/strain fields being computed simultaneously. Validation was performed using the total upset, temperature (pyrometer) measurements and welding time. Their later work (Moal and Massoni, 1995) included further validation using the rotational speed. In spite of the model potential, it was not further tested nor validated. Later, D'Alvise *et al*. developed a two-dimensional coupled thermomechanical IFW model using FORGE2®, which is capable of predicting the temperature, stress/strain fields and residual stresses in similar and dissimilar welds (D'Alvise *et al*., 2002). The model used the same heat-generation scheme as the previous model. However, the model was only validated using temperature measurements, the weld upset, flash morphology and the rotational speed, with reasonable agreement between the model's prediction and experimental data. Nonetheless, some features of the reported model were not discussed or validated (e.g. residual stresses and plastic strains), while the microstructural development was not even considered.

Following the earlier models, several researchers utilised available FE packages (e.g. MSC Marc and DEFORM 2D) to model the thermal and stress/strain fields due to IFW, yet model validation was always limited (mostly thermal, rotation speed and weld morphology) without considering the microstructure nor the residual stress development (Fu *et al*., 2003; Jeong *et al*., 2007; Liwen *et al*., 2004). Yet, with the advance in electron microscopy

and in residual stress characterisation using neutron diffraction, it became possible to further validate the FE models using the residual stress predictions with measured stress profiles (Grant *et al*., 2009; Wang *et al*., 2004, 2005).

The work by Wang *et al*. focussed on modelling the residual stress development in RR1000 (a high γ' Ni-based superalloy) welds using DEFORM, and comparing it with residual stress data obtained using neutron diffraction (Wang *et al*., 2004, 2005). Their energy-input FE models were two-dimensional axisymmetric models, with a visco-plastic material model and using a frictional heat flux (q), which is given by:

$$q(t) = \frac{1}{2}\frac{\eta}{A}\frac{dE}{dt} = \frac{1}{2}\frac{\eta}{A}\frac{d\left\{\frac{I\omega^2(t)}{2}\right\}}{dt} = \frac{1}{2}\frac{\eta}{A}I\omega(t)\frac{d\left(\omega(t)\right)}{dt} \qquad [2.12]$$

where η is the efficiency, A is contact interface area, I is the moment of inertia, ω is the rotational velocity and t is the time. The model used the calculated thermal fields to perform the residual stress analysis by performing creep (elastic) analysis during cooling. Generally, the predicted trends matched the measured ones, whereby a bending moment was predicted in the axial direction, while the hoop direction showed very high stress levels that approached the yield strength, compared with the radial direction that showed minimal stresses. Nonetheless, the predictions were ~15–35% higher than the measured stresses, which was attributed to the lack of high temperature creep data (>750°C) and the influence of the flash machining (Wang *et al*., 2005). Further validation was also performed through microstructural characterisation of the γ' precipitates development in three different welds, and comparing it with the model thermal predictions. The work of Wang *et al*. was further improved by Grant *et al*. (2009), using a larger material property database (up to 1150°C), better representation of the heat generation model and the forging force application, and using an elasto-plastic analysis of the stress development. Validation of the model was performed using microstructural characterisation of base-metal specimens that were thermally cycled using the model predictions, and the residual stress measurements. The predicted residual stresses were both spatially and quantitatively similar to the measured stresses, especially in the hoop direction, although the model failed to predict the axial stresses with the same accuracy (Fig. 2.10). The radial stresses were generally negligible, especially considering the accuracy in the stress analysis using neutron diffraction (±70 MPa).

Grant *et al*. also used their model to perform parametric simulations investigating the influence of the forging pressure on the thermal fields. It

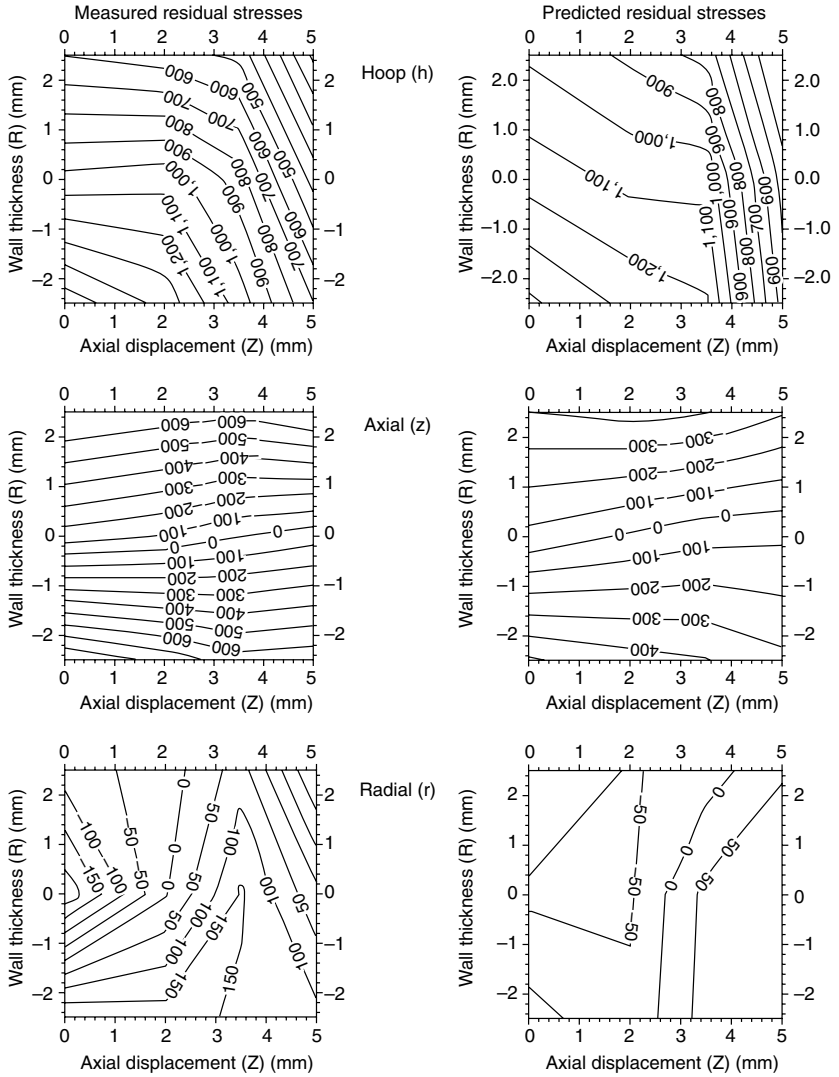

2.10 A comparison between the measured and predicted residual stresses in RR1000 IWs using Grant *et al.* model (2009).

was found that the increase in the forging pressure leads to a slight increase in the maximum temperature, resulting in steep thermal gradients (Fig. 2.11a). Nonetheless, by calculating the residual stress development, it was evident that the increase in pressure only affected the location of the maximum hoop stress resulting in a narrower heat-affected zone (HAZ), but did not affect the maximum stress quantity (Fig. 2.11b).

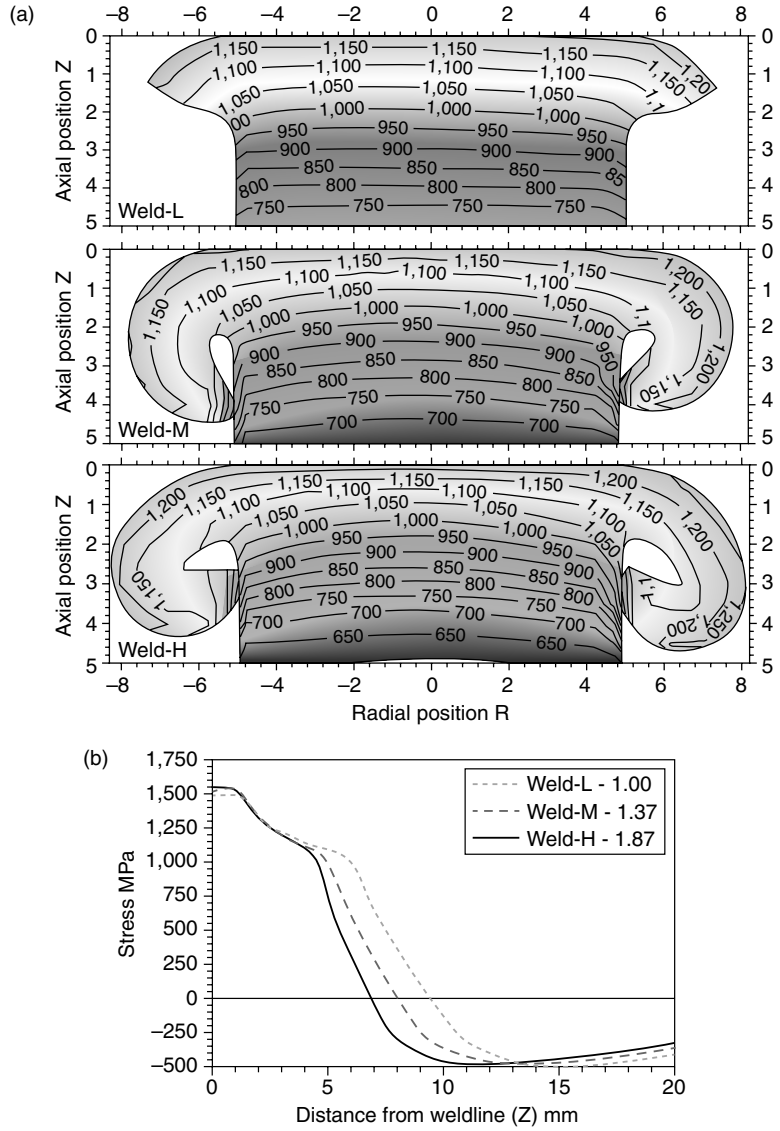

2.11 Influence of the forging pressure on (a) the thermal fields and (b) hoop stress (forging pressure low (L), medium (M) and high (H)) (Grant *et al.*, 2009).

Recent IFW modelling reports used new numerical approaches (e.g. Eigenstrain FE modelling (Korsunsky, 2009)), but still focus on Ni-based superalloys welds. There are only a limited number of reports on IFW models when joining other materials than Ni-based superalloys. In ferritic steels, a phase transformation occurs during cooling after welding (e.g. martensitic or bainitic

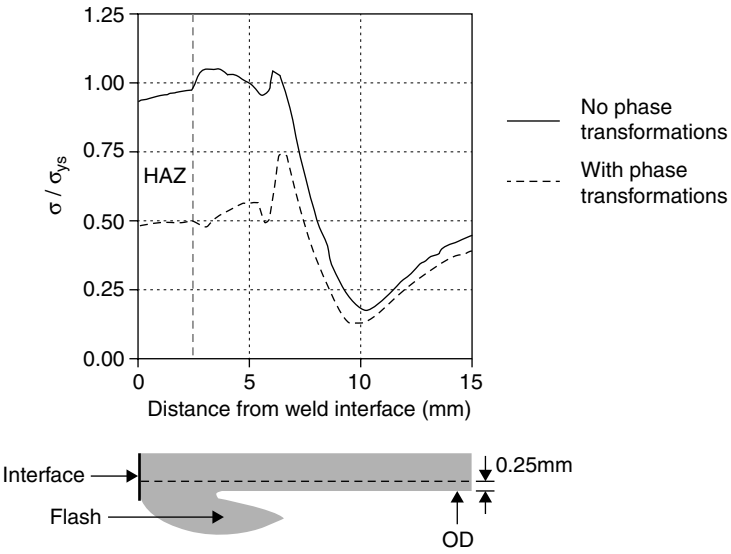

2.12 Influence of the phase transformation on the von Mises residual stress distribution (Bennett *et al.,* 2007).

transformation), resulting in a volumetric change affecting the residual stress evolution in this region (Moat *et al.*, 2009). In their model, Bennett *et al.* studied the residual stress development in SCMV steel welds using a DEFORM 2D model (Bennett *et al.*, 2007), validated using the rotation speed, upset and thermocouple measurements. At the end of the IFW cycle, the residual stress development was traced throughout the martensitic transformation, where the fraction transformed and a volumetric change parameter were calculated, which was then used to investigate the influence of the transformation on the residual stress development. Their findings showed that the occurrence of the transformation resulted in a significant drop in the residual stresses owing to the volumetric increase during cooling (Fig. 2.12). Although this model is the first to investigate the influence of the phase transformation on the residual stress development, the residual stress capability was not validated.

2.3 Microstructural development

Because of the nature of IFW, the resulting joint demonstrates a unique yet localised microstructural residual stress, and mechanical properties develop across the joint. Although it is generally believed that CDFW and IFW result in a similar microstructural development (Kallee *et al.*, 2003), early IFW literature suggested that the use of the flywheel results in circumferential flow lines at the weld plane, compared with radial flow lines in non-flywheel welds (Oberle *et al.*, 1967). It was argued that such a metallurgical difference

would result in better fatigue properties of IFW welds owing to the spiralling of the flow lines that become almost tangential to the surface, compared with being normal to the surface in CDFW. Nonetheless, no comparative studies have ever been performed to quantitatively assess the metallurgical differences between IFW and CDFW to date. In the following sections, the influence of IFW on the microstructural development in Ni-based superalloys, titanium alloys, steels and aluminium alloys will be discussed.

2.3.1 Nickel-based superalloys

The majority of the microstructural studies on Ni-based superalloy inertia friction welds focussed on the development of the precipitate structure in commonly used aerospace alloys, especially RR1000, IN718, U720Li, Astroloy, and Waspaloy (Table 2.1).

According to Adam (1982), inertia friction welds of Ni-based superalloys can be classified into five regions from the centre outwards (based on Astroloy):

- Fine grain region: this is the weld line where dynamic recrystallisation occurs.
- Deformed and rotated grain region: where the intense plastic deformation leads to the rotation and re-orientation of the grains.
- Deformed grain region: where plastic deformation has occurred, without rotating the grain structure.
- HAZ: where the material is only thermally affected.
- Base (unaffected) metal: where the material is thermally and mechanically unaffected.

Conversely, Preuss *et al*. (2002a) found in RR1000 IFWs that weld-line microstructure is actually not heavily deformed, showing coarse recrystallised grain structure, followed by fine grains within 0.5 mm of the weld line. Beyond the central region, the material was plastically deformed, with the temperature insufficient to lead to recrystallisation.

Table 2.1 Chemical compositions (wt %) of selected aerospace Ni-based superalloys

Alloy	Ni	Cr	Co	Mo	W	Nb	Ti	Al	Fe	C	Other
RR1000	52.3	15.0	18.5	5.0	–	–	3.6	3.0	-	0.027	0.015B, 2Ta, 0.06Zr, 0.5Hf
Astroloy	56.5	15.0	15.0	5.25	–	–	3.5	4.4	<0.3	0.06	0.03B, 0.06Zr
U 720Li	57.0	16.0	15.0	3.0	1.25	–	5	2.5	-	0.025	0.03Zr
IN718	52.5	19.0	-	3.0	–	5.1	0.9	0.5	18.5	0.08	0.15 max Cu
Waspaloy	57.0	19.5	13.5	4.3	–	–	3.0	1.4	2.0	0.07	0.06B, 0.09Zr

Source: Donachie and Donachie, 2002.

Owing to the nature of the precipitation strengthening mechanism in Ni-based superalloys, several IFW studies investigated the development of the γ' precipitate (Ferte, 1993; Huang *et al*., 2007; Preuss *et al*., 2002a, 2004, 2006; Soucail *et al*., 1992; Wang *et al*., 2005), and γ'' precipitate (Huang *et al*., 2007; Preuss *et al*. 2006; Roder *et al*., 2005, 2006) structures using scanning electron microscopy (SEM), transmission electron microscopy (TEM) and synchrotron X-ray diffraction. Limited studies investigated the development of grain boundary (GB) carbides/borides (Ferte, 1993; Montay *et al*., 2007) and microtexture (Preuss *et al*., 2002a). Qualitatively, Huang *et al*. investigated the precipitate development at the vicinity of the weld region in a IN718-U U720Li weld using SEM and TEM (Huang *et al*., 2007). In the IN718 side (Fig. 2.13), it was clear that the thermal fields experienced during welding led to complete dissolution of the γ'', γ', or δ precipitates as far as 2.1 mm from the weld centre, and also created a low dislocation density structure. This led to a hardness drop observed in the IN718 side of the weld. At 4 mm from the weld centre, evidence of the presence γ'' precipitate was found. Similar observations were reported by Roder *et al*., who investigated the extent of dissolution of the γ'' and δ phase (Ni_3Nb phase for grain-size control), (Roder *et al*., 2005). It was reported that whereas the γ'' phase was fully dissolved up to ~500 μm from the weld centre, the δ phase was dissolved up to only ~300 μm from the weld centre.

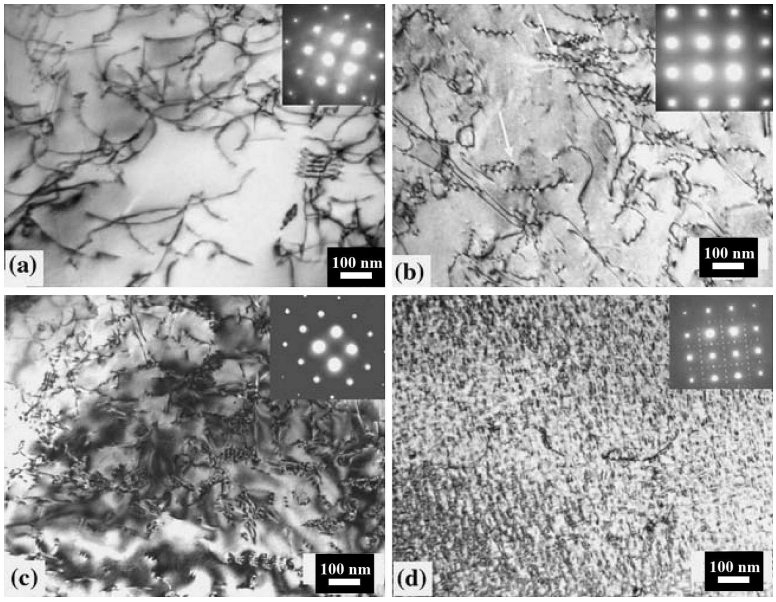

2.13 The γ'' precipitate development in IN718 (AW) at (a) 0.2 mm, (b) 0.7 mm, (c) 2.1 mm and (d) 4 mm from the weld line (Huang *et al.*, 2007).

In highly γ'-strengthened alloys (Astroloy (Soucail *et al*., 1992), RR1000 (Preuss *et al*., 2002a), and U720Li (Huang *et al*., 2007)) a different development in the weld centre was observed owing to the fast precipitation kinetics of γ' and the high levels of γ'' stabilisers (this excludes Waspaloy). For instance, at the weld centre U720Li IFW, a high fraction of reprecipitated γ' was observed (Fig. 2.14a), which has decreased dramatically only 1 mm from the weld line (Fig. 2.14c) (Preuss *et al*., 2004).

Preuss and co-workers used both synchrotron X-ray diffraction and image analysis to map the γ' and γ'' fraction development in RR1000, IN718, and U720Li IFWs across the weld line (Huang *et al*., 2007; Preuss *et al*., 2002a, 2004, 2006). It was evident that IFW led to the dissolution of the strengthening precipitates in the weld region, which ranges from full dissolution of γ'' in the case of IN718, to dissolution and reprecipitation of γ' in RR1000 and U720Li (Fig. 2.15). These measurements show that IFW disturbs the precipitate volume fraction within a region of ±3 mm from the weld line, resulting in hardness peaks caused by reprecipitation during cooling in the presence of a strong driving force for reprecipitation in RR1000 and U720Li, or hardness troughs caused by partial or full dissolution (Preuss *et al*., 2002a).

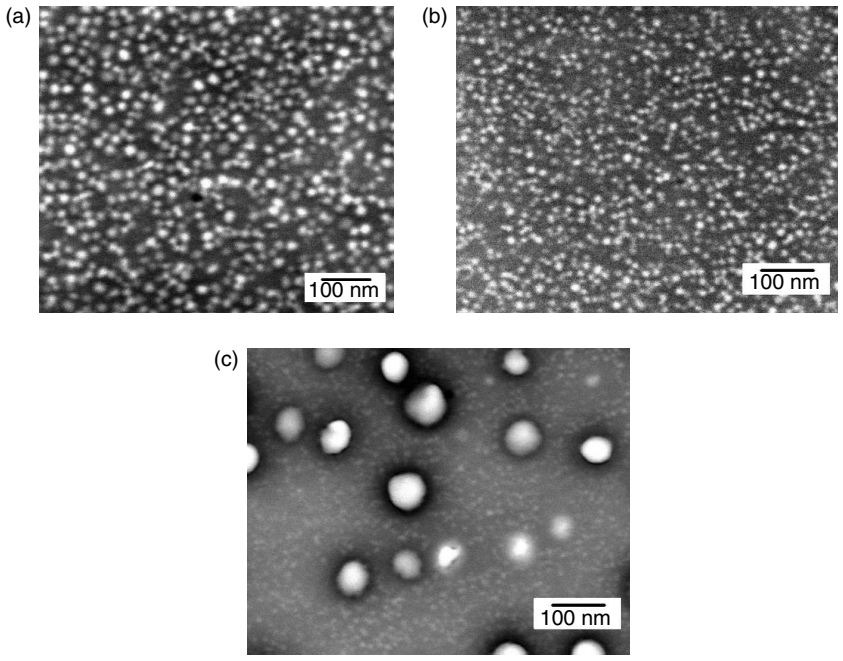

2.14 The γ' precipitate development in U720Li (AW) (a) at the weld line, (b) 0.5 mm and (c) 1 mm from the weld line (Preuss *et al.,* 2004).

By correlating the γ' distribution with the microhardness distribution in RR1000 (Preuss *et al*., 2002a) and U720Li (Preuss *et al*., 2004), it becomes evident that the hardness variation is controlled by a combination of strengthening mechanisms (precipitate strengthening, GB strengthening and work hardening), as correlated through measurements of the grain size, tertiary γ' volume fraction and γ/γ' misfit, although the contributions of these effects have not been quantified (Preuss *et al*., 2002a). In inertia friction welded Astroloy, Soucail *et al*. (1992) found a high dislocation density, with tangled dislocations, Orowan loops and sheared particles with varying extents depending on the distance from the weld centre. Electron backscatter diffraction (EBSD) maps also showed regions of high stored energy about 1 mm from the weld line in inertia friction-welded RR1000 (Preuss *et al*., 2002a). This demonstrates that a region exists adjacent to the recrystallised region where material has been deformed significantly, but the stored energy was not sufficient to result in dynamic recrystallisation.

In addition to the microstructural investigations of the precipitate structure, other microstructural features of interest include the development of the GB carbides (Ferte, 1993; Montay *et al*., 2007). The high temperature experienced during welding (~1200°C) is sufficient to dissolve (fully or partially) any existing carbides, which subsequently reprecipitate at the grain boundaries during cooling or post-weld heat treatment (PWHT). The morphology of the GB carbides has a strong influence on the ductility and fatigue properties, where discrete or globular carbide particles are beneficial as they act as obstacles for GB motion, while continuous carbide films are

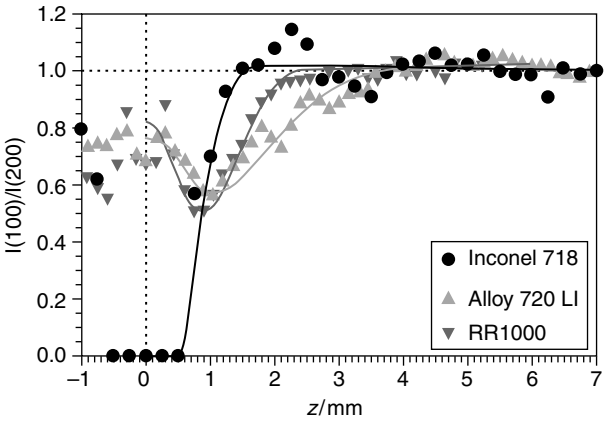

2.15 The normalised integrated intensity (±0.04 accuracy) of the γ' superlattice reflection as a function of the distance from the weld line (z) in the AW condition of IN718, 720Li and RR1000 IWs (Preuss *et al*., 2006).

harmful (Li *et al*., 2007). Li *et al*. detected the formation of continuous films of $M_{23}C_6$ carbides with a relatively high Cr content close to the weld region within the primary γ'-free zone in the U720Li side of a IN718-U720Li IFW following PWHT (Li *et al*., 2007) (Fig. 2.16). As it is known that the high Cr content of the carbides results in a localised depletion of Cr in their vicinity, this is expected to result in poor oxidation damage resistance in these welds. The formation of the carbides was reported to have a negative influence on the fatigue-crack propagation (FCP) properties of Ni-superalloy welds as will be discussed later (Daus *et al*., 2007; Li *et al*., 2007).

It was suggested that performing a solution-plus-aging treatment to redistribute the carbides could solve the problem of the continuous GB carbides. Following this approach, Ferte compared three PWHT conditions in N18 IFWs, where it was found that on increasing the PWHT time from 4 to 8 h at 800°C, grain boundaries became increasingly decorated with Cr-Mo carbides (Ferte, 1993). However, on performing a solution treatment plus aging PWHT, a bimodal γ' precipitate structure was obtained in the weld centre,

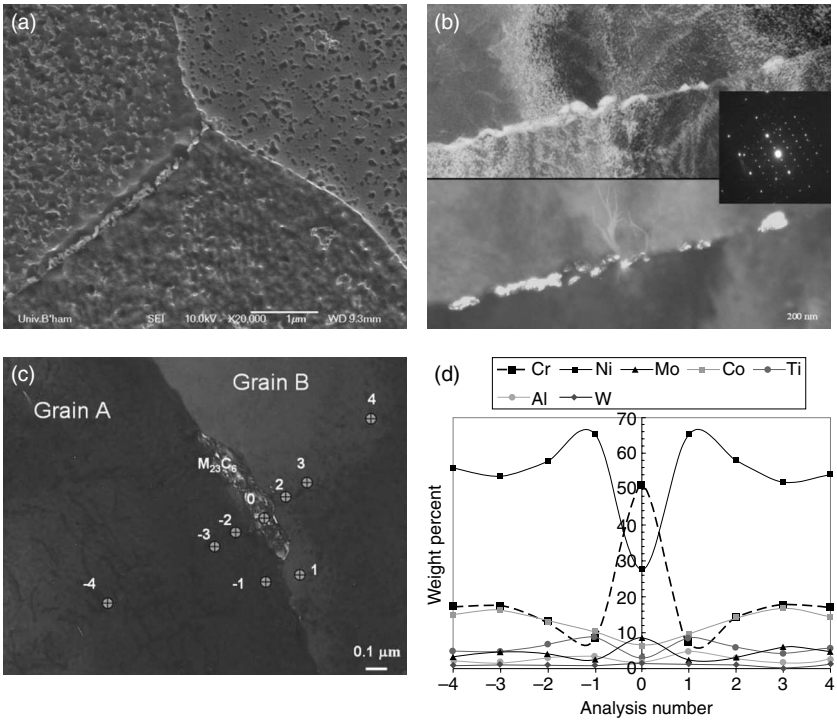

2.16 GB carbides ($M_{23}C_6$) precipitation in 720 Li in the primary γ' free zone following PWHT (a) SEM, (b) bright and dark-field TEM with SAD pattern, (c) and (d) chemical analysis across a carbide particle (Li *et al.*, 2007).

whose sizes are similar to those of the parent metal. Although this latter treatment led to a significant improvement in the FCP resistance, it also led to large grain growth in the HAZ, which can be attributed to the large stored energy present in some parts of the HAZ. It is also worth noticing that a solution heat treatment of large welded components is economically not viable.

2.3.2 Steels

The majority of the microstructural studies on steel IFW dealt with ferritic steels. During IFW of ferritic steels, the temperature of the material at the interface exceeds the austenisation temperature, which, alongside the thermomechanical deformation, results in a very unique microstructure and texture. The temperature decreases gradually from the weld centre towards the HAZ and the parent metal. Upon cooling, the microstructure shows varying amounts of ferrite, martensite, bainite or retained austenite across the weld regions, depending on the cooling rates and the stresses.

Among the most notable IFW applications in the aerospace industry is the dual drive shaft (dissimilar SCMV-AerMet100 IFW joint) (Moat *et al*., 2008, 2009; Robotham *et al*., 2005), which received the most thorough characterisation among the ferrous welds. SCMV (0.3% C, 3.15% Cr, 1.6% Mo, 0.1% Va, 0.6% Si) is used at the turbine (high-temperature) end of the aero engine drive shaft, while Aermet 100 (0.2% C, 2.5% Cr, 10.1% Ni, 12.7% Co, 1.37% Mo, 3.26% Nb, 0.01% Mn) is used at the compressor end of the shaft, where a high-strength alloy is required to withstand the high torque (Robotham *et al*., 2005). Moat *et al*. (2008) divided the weld into four regions (Fig. 2.17):

- the weld (bond) line (interface): where a slight banding between the two alloys was observed, yet without full mixing

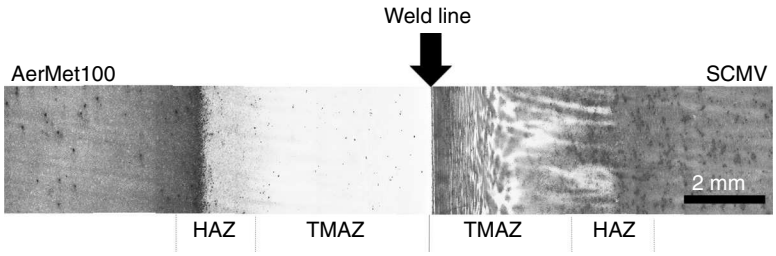

2.17 Microstructural zones in the AerMet100-SCMV IW. (Courtesy of R. J. Moat.)

- the (partially or fully) deformed zone or the thermomechanically affected zone (TMAZ): where varying thermomechanical effects result in the deformation of the parent microstructure, but not to annihilate it completely
- the HAZ: where the microstructure experiences only thermal effects, resulting in the formation of a recrystallised equiaxed grain structure, with some coarsening (Robotham *et al*., 2005)
- the unaffected parent metal.

The width of the regions is dependent on the process parameters with the forging pressure having a major impact on HAZ (high pressure narrows HAZ) and TMAZ (high pressure increases extent of deformation). Conversely, the increase in the rotation speed (also weld energy) widens the HAZ accompanied with a relatively coarse grain morphology. As a result, a two-stage pressure can be occasionally used to refine the grain structure, by applying a higher pressure following the stop of the spindle (Robotham *et al*., 2005).

It is known that IFW creates a heterogeneous microstructure, with varying quantities of the phases present (e.g. martensite, bainite or retained austenite) (Tumuluru, 1984). Thus, it is necessary to quantify the extent of the microstructural heterogeneity, especially the presence of retained austenite and martensite, owing to their influence on the mechanical properties. Laboratory and synchrotron X-ray diffraction was used by Moat *et al*. (2008) to map the austenite fraction variation across the weld in the as-welded (AW) and PWHT conditions of before-mentioned SMCV/AerMet100 IFWs (Fig. 2.18). A significant variation in the retained austenite was found especially towards the AerMet100, whereby the volume fraction decreased from ~7–9% in the parent AerMet100 to ~2–4% within the HAZ, prior to reaching 8–9% within the TMAZ. In the SCMV side, there is a pronounced localised increase in the austenite fraction (~8%) within the TMAZ, while keeping the ferrite-cementite structure within the parent metal and HAZ. The high austenite fraction in the TMAZ of both sides was attributed to the rapid cooling, resulting in the retention of some austenite, with varying amounts because of the difference between both alloys in the austenite stabilisers content. In the HAZ, the temperature was insufficient to fully austenise the SCMV side, which resulted in the absence of austenite. Following PWHT, the SCMV side regained the ferrite-cementite structure in all its regions. In the AerMet100 side, the overall austenite content decreased owing to PWHT, yet without changing the local variation across the different regions. Further microstructural evidence was obtained using electron microscopy, which showed that the SCMV TMAZ AW microstructure was predominantly martensitic with some retained austenite, as manifested in

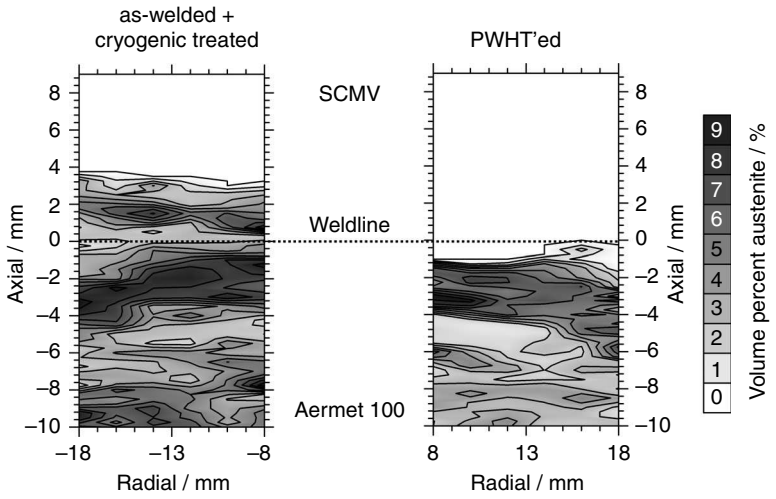

2.18 A two-dimensional map for the austenite fraction in SCMV-AerMet100 IWs (AW and PWHT conditions) as measured by high-energy synchrotron X-ray diffraction (Moat *et al.*, 2009).

the laths and the absence of carbides. In the AerMet100, the thermal exposure led to some precipitation of the M_2C carbides, with varying degrees. These complicated developments resulted in a unique microhardness development as will be discussed in the section 'Microhardness development'.

2.3.3 Titanium alloys

The microstructural investigations of inertia-friction-welded aerospace titanium alloy are very limited, and do not provide sufficient information on the several classes of titanium alloys (α, α+β and β alloys). Among the earliest reports on IFW of α+β titanium alloys, Nessler *et al*. performed preliminary microstructural investigations of Ti-8Al-1V-1Mo and Ti-6Al-4V (Nessler *et al*., 1971). No evidence of melting was found, although a narrow alpha-case region was observed at the centre of the flash. Generally, the weld region was narrow (~3 mm) and mostly composed of a highly deformed structure with fine grains. At the weld centre, martensitic α' was observed, which apparently resulted from rapid cooling from above the β-transus temperature (~1000°C). In a different investigation, the HAZ microstructure in Ti-6Al-4V IFW was also found to contain Widmanstätten α (transformed β grains) (English, 1995). Similarly, inertia friction welded Ti-6Al-2Sn-4-Zr-2Sn also displayed a refined lamellar α structure in the weld region (Barussaud and Prieur, 1996).

Baeslack III *et al*. studied an IFW of a rapidly solidified titanium alloy (Ti-6.4Al-3.2Sn-3.0Zr-2.7Er -2.5Hf-1Nb-0.33Ge-0.3Ru-0.15Si) (Baeslack III *et al*., 1991). The weld regions were classified into an inner heat and deformation zone (HDZ), which is ~25 μm wide with dynamically recrystallised fine β grains with fine Er-rich dispersoid (100–350 nm) precipitates along the grain boundaries and an outer HDZ (~500 μm wide) that contained transformed β grains with α colonies. The unique composition of this experimental alloy makes it difficult to generalise the findings of this study.

A single report by Roder *et al*. (2003) is available on the microstructural development of inertia-friction-welded Ti-6Al-2Sn-4Zr-6Mo, an α+β Ti alloy that is more heavily β-stabilised than Ti-6Al-4V. Upon welding, four unique microstructural zones were observed (Fig. 2.19):

- region I (centre to 175 μm): showing recrystallised β grains (~20 μm in size)
- region II (175–275 μm): showing recrystallised β grains (~10 μm in size), and deformed β grains (>20 μm in size), which are elongated, in the radial direction
- region III (275–525 μm): showing deformed β grains similar to those in region II
- region IV (525–1500 μm): showing a deformed parent microstructure.

An interesting feature in Ti-6246 IFWs is the observation of the so-called ghost α plates in region III, which are α_P plates from the base metal that was heated up to the β-phase field, without allowing sufficient time for diffusion to homogenise the chemical composition. Following PWHT, fine α needles precipitated within the β grains in all the regions (I–IV).

It is important to note that the publically available investigations do not provide detailed information on the microstructure development in inertia-friction-welded titanium alloy. Several alloys need to be further investigated (e.g. Ti-64 and Ti-6246) and the feasibility of welding alloys such as Ti-5553

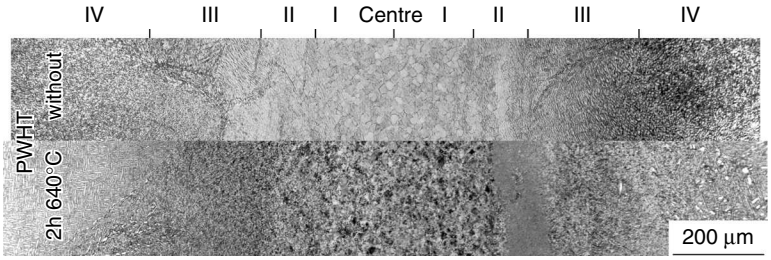

2.19 Microstructural zones in a Ti-6246 IW (AW and PWHT) (Roder *et al.*, 2003).

need to be pursued to increase the opportunities of using titanium IFW in the aerospace industry.

2.3.4 Other alloys

There are few preliminary reports in the literature on the weldability of other alloys using IFW, including B2 aluminides (Whittenberger *et al*., 1987), aluminium-based alloys (Hou and Baeslack III, 1990; Koo *et al*., 1991), metal-matrix composites (Lienert *et al*., 1996) and dissimilar welds (Jeong *et al*., 2007; Zhu *et al*., 2009). The interest in iron and nickel aluminides as potential high-temperature materials in the mid-1980s led to an interest in performing investigations of their weldability. Whittenberger *et al*. (1987) investigated a dissimilar FeAl and NiAl IFW. In contrast to fusion welding, IFW of these alloys did not lead to cracking or porosity formation, but instead it was composed of fine equiaxed grains. Nonetheless, upon performing post-weld annealing at 1027°C for 16 h, recrystallisation occurred leading to grain coarsening, which was detrimental for high-temperature creep strength. This initial report was never followed by any other investigations for the metal aluminides.

Preliminary studies were performed in the early 1990s to investigate the inertia friction weldability of rapidly solidified alloys, Al-Fe-Mo-V (Hou and Baeslack III, 1990) and Al-Fe-V-Si (Koo *et al*., 1991), which involved microstructural characterisation of the weld regions using electron microscopy and mechanical testing. This work was further extended by studying SiC-reinforced Al-Fe-V-Si alloy, which showed that composites are also weldable using IFW. Nonetheless, beyond these studies, the interest of IFW of Al alloys has not been revived again for over a decade.

There has been some recent interest in investigating the weldability of dissimilar superalloy-steel IFWs. Jeon *et al*. performed a preliminary microstructural and mechanical property characterisation of a Nimonic 80A/SNCrW IFW (Jeong *et al*., 2007). Although there is a lack of extensive mixing at the weld interface, the welds had mechanical properties (strength and fatigue) better than the properties of SNCrW. In another report, Zhu *et al.* (2009) investigated a Nimonic 80A/4$Cr_{10}Si_2Mo$ dissimilar weld using electron microscopy. Chemical analysis by X-ray spectroscopy was used to characterise the extent of mixing at the weld interface that showed that there is a central mixing zone (equivalent to the weld line) of ~100 μm width. The weld line was composed of austenite grains of 3–5 μm size, with fine carbides (50 nm in size). Beyond the mixing region, a high dislocation density region was found, similar to that described earlier for inertia-friction-welded Ni-based superalloys called, in this case, the pure shearing region.

As it was discussed, the studies on alloys other than Ni-based superalloys, steel and titanium are very limited. Although IFW is known to have been applied to other aerospace materials, the majority of the welds produced are mostly for Ni-based superalloys, and only recently on steel and titanium. Further work is needed to investigate the utility of IFW in welding new aerospace materials and particularly the ability to join dissimilar metals and alloys.

2.4 Development of mechanical properties

2.4.1 Ni-based superalloys

Microhardness development

Owing to the nature and the volume fraction of the strengthening phases, differences in the microhardness distribution were observed between inertia friction welds of advanced Ni-based alloys with a high γ' volume fraction (e.g. RR1000, U720Li, etc.) and welds of superalloys with a volume fraction of about 20–25% precipitates, such as Waspaloy and the $\gamma'+\gamma''$-strengthened IN718. In general, the latter class of superalloys tends to display a significant hardness trough in the weld region in the AW condition, towing to either a complete absence or at least significantly reduced volume fraction of strengthening precipitates (Waspaloy Fig. 2.20a) (Adam, 1982; Roder *et al.*, 2005). However, in alloys with γ'-volume fractions around 40–50% (e.g. RR1000 (Preuss *et al.*, 2002a, 2006), N18 (Ferte, 1993), U700 (Adam, 1982), U720Li (Preuss *et al.*, 2004, 2006) and Astroloy (Ferte, 1993), with ~50% γ'), both the region close to the weld centre and the HAZ show hardness peaks even in the AW condition (RR1000, Fig. 2.20b). This behaviour was attributed to the higher levels of γ'-stabilising alloying elements such as Al and Ti found in such alloys compared with, for example, Waspaloy providing a high driving force of γ' reprecipitation during rapid cooling following welding (Preuss *et al.*, 2002a). However, a small hardness trough, as shown in Fig. 2.20b, can still be observed attributed to the partial γ' dissolution during welding not providing a sufficiently high driving force for reprecipitation during cooling. Following PWHT in γ'-rich alloy inertia friction welds, additional γ' precipitation occurs resulting in an overall increase in hardness, with the maximum hardness occurring towards the weld centre (tertiary γ'), and decreasing towards the base metal with a change in the slope in the previously observed hardness trough in the AW condition (Fig. 2.20b) (Preuss *et al.*, 2002a). Similar PWHT hardness trends were observed in other γ'-rich alloys inertia friction welds (e.g. U700 (Adam, 1982), U720Li (Preuss *et al.*, 2004, 2006), and N18 (Ferte, 1993)).

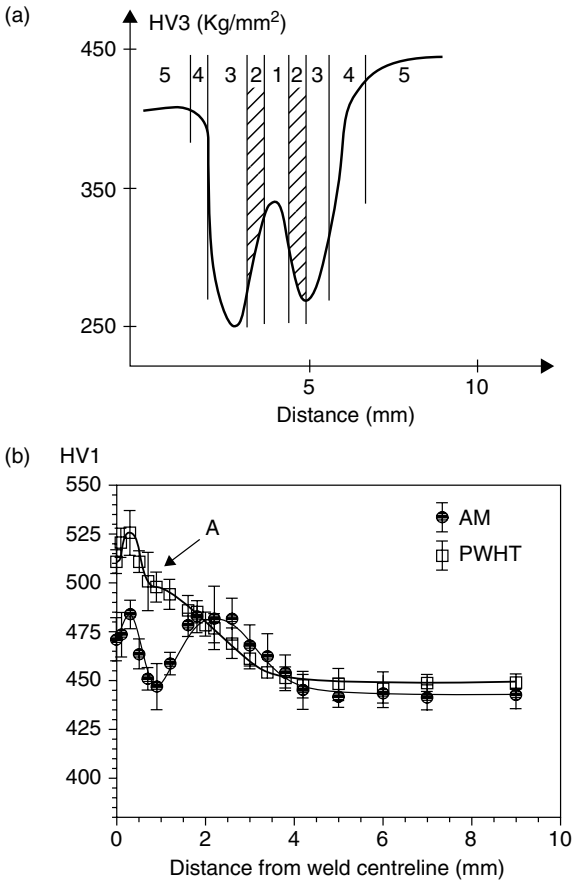

2.20 The effect of the γ' content on the microhardness development (mid-thickness) in IFWs of Ni-based superalloys: (a) low γ' Waspaloy (Adam, 1982), and (b) high γ' RR1000 (Preuss, 2002a).

In the $\gamma'+\gamma''$-strengthened alloy IN718 following a PWHT, the hardness of the weld region is either slightly or fully regained depending on whether a low temperature anneal or a complex multistage PWHT was undertaken (Fig. 2.21) (Roder *et al.*, 2005). In fact, the latter PWHT led to a slight hardness increase in the weld region compared with the base metal, which was attributed to superposition of precipitate and grain-size strengthening.

In dissimilar inertia friction welds, Daus *et al.* (2007) studied the influence of the process parameters on the hardness development in RR1000-IN718 welds. Three welds were investigated, representing different parameter combinations (Fig. 2.22a). It was evident that the hardness traces created a combination of the typical trends in the welds of γ' and $\gamma'+\gamma''$-strengthened alloys as previously discussed, with the RR1000 side showing two peaks

with a small trough in between, while the IN718 side showed a significant hardness trough in the weld region. The dissimilar hardness trend following PWHT was observed in U720Li-IN718 welds (Huang *et al.*, 2007) (Fig. 2.22b). Following PWHT, the hardness of the weld region (±6 mm from the weld centreline) generally increased to a maximum of ~550 H_V in the U720Li side and ~490 H_V in the IN718 side, with the weld region in each side showing hardness values above its respective base metal. It was also found that the increase in PWHT time led to the parent IN718 being overaged, while the hardness of the U720Li side remained roughly unchanged. It was generally recommended that PWHT of IN718 is performed either by full annealing at 955°C to avoid heterogeneous aging effects (Donachie and Donachie., 2002), or below 732°C to maximise the weld strength. However, U720Li requires significantly higher temperatures between 760°C (Huang *et al.*, 2007) and 1135°C (Donachie and Donachie., 2002) to relieve the high stresses that result from the welding process. This highlights one of the fundamental issues when joining Ni-base superalloys with different temperature capability. While a low-temperature PWHT might avoid overaging of the alloy with the comparatively low temperature capability, such heat treatment is unlikely to be effective in terms of relieving residual stresses in the alloy with high-temperature capability. In contrast, if the high-temperature alloy guides the PWHT procedure, it is likely that the 'low'-temperature alloy will get overaged resulting in low strength. This demonstrates the importance of considering microstructure/mechanical property development together with residual stress mitigation particularly in dissimilar welds when identifying appropriate PWHTs. Further dissimilar microhardness traces for IN718-X (X: U720Li, Incoloy909, René88) including the influence of different PWHT, can be found in the work of Roder and co-workers (Roder *et al.*, 2005, 2006).

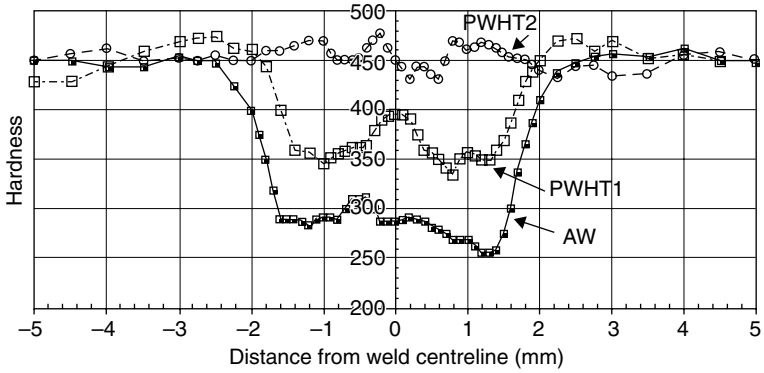

2.21. Microhardness distribution (mid-thickness) in $\gamma'+\gamma''$-strengthened IN718 (Roder *et al.*, 2005).

Tensile properties

To measure the cross-weld mechanical properties, Preuss *et al.* used electron speckle-pattern interferometry (ESPI) to measure the proof-stress distribution across the weld in IN718, RR1000 and U720Li alloys IFWs (Preuss *et al.*, 2006) (Fig. 2.23). The distribution shows a soft-weld region in IN718, with a yield strength of ~650 MPa. Although the proof-stress traces agree qualitatively with the microhardness profiles, they provide further quantitative information on the local tensile properties of the weld regions. To investigate the effect of the test temperature, Roder and co-workers measured the PWHT tensile strength and ductility in similar and dissimilar

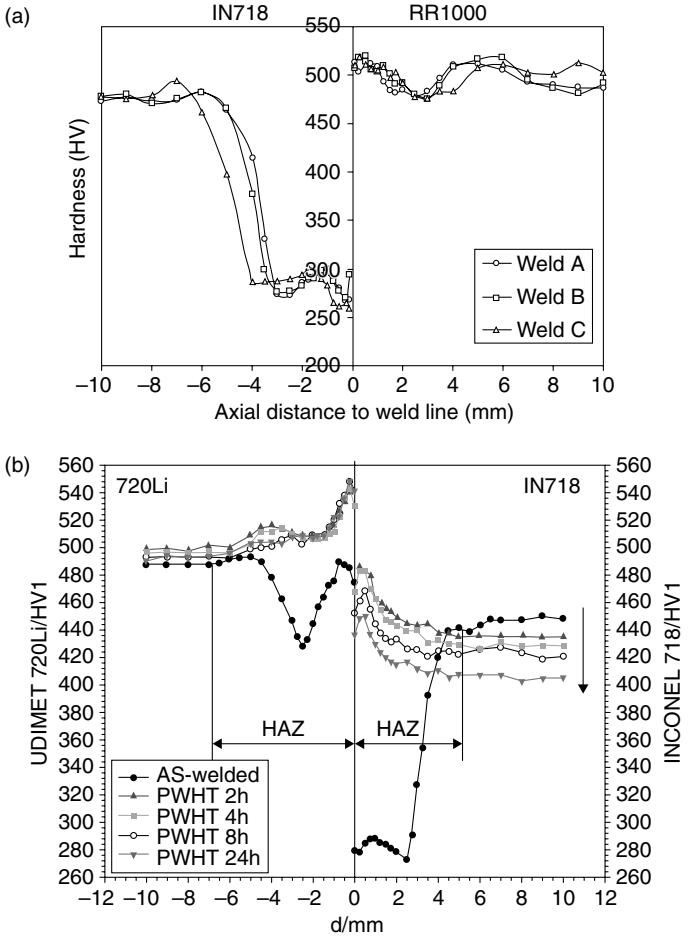

2.22 Hardness distribution in dissimilar IN718-X IFWs. (a) IN718-RR1000 (AW) (Daus *et al.*, 2007), (b) U720Li-IN718 (Huang *et al.*, 2007).

IN718 welds (Roder *et al.*, 2005, 2006). It was found that failure generally occurred in the IN718 side of the weld, except for Incoloy909 alloy. A drop in tensile strength (200–300 MPa from strength at 20°C) was observed for IN718 welds tested at high temperature (650°C), yet strength was generally within the typical range for IN718. However, in IN718-U720Li welds failure occurred at strength levels below the typical levels for IN718 and U720Li regardless of the PWHT parameters.

Fatigue-crack propagation (FCP)

Limited work is available on the FCP measurements in similar Ni-superalloy inertia friction welds, with a single report on N18 welds (Ferte, 1993). The majority of FCP measurements in Ni-superalloys inertia friction welds were performed on dissimilar IN718-X welds (X: RR1000 or U720Li) (Daus *et al.*, 2007; Li *et al.*, 2007). The FCP studies investigated the influence of the PWHT parameters (Ferte, 1993), test temperature (Daus *et al.*, 2007; Montay *et al.*, 2007) and the local FCP rates in different weld regions (Montay *et al.*, 2007). For more general information on FCP in Ni-based superalloys (especially RR1000), the reader is directed to other references (Everitt *et al.*, 2007; Knowles and Hunt, 2002; Starink and Reed, 2008). Ferte (1993) showed that the PWHT parameters significantly affect the FCP rates in N18 IFWs. By increasing the PWHT duration from 4 to 8 h at 800°C, the FCP rates decreased owing to the precipitation of (Cr,Mo)-rich carbides along the grain boundaries. By introducing a post-weld solution stage at 1165°C for 4 h in the process, roughly full retention of the parent FCP rates was observed in the welded sections (Fig. 2.24a), which was attributed to the formation of a similar microstructure

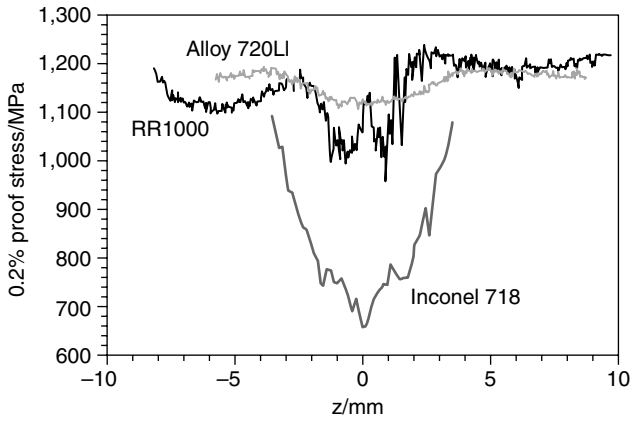

2.23 Proof-stress (0.2%) distribution in AW IFWs of IN718, RR1000, and 720Li (average accuracy ±10–50 MPa) (Preuss *et al.*, 2006).

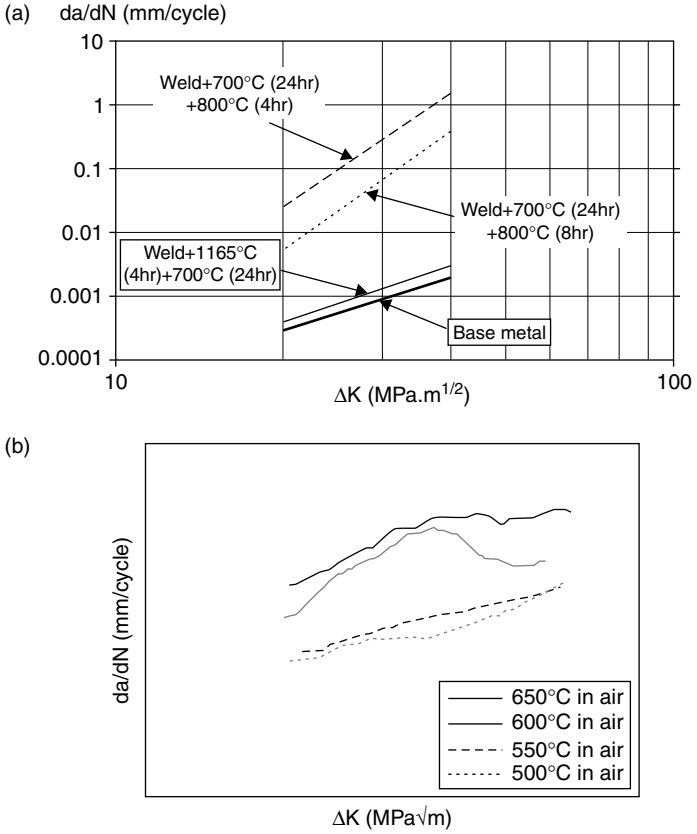

2.24 FCP in Ni-superalloy inertia friction welds, showing the influence of (a) PWHT tested at room temperature and (b) the test temperature (following PWHT). (a) N18 (Ferte, 1993), (b) RR1000-IN718 (Li *et al.*, 2007).

to that of the parent metal. To consider the influence of the test temperature, Li *et al.* found that the FCP rates increased with the increase in temperature in RR1000-IN718 PWHTed welds (Li *et al.*, 2007) (Fig. 2.24b). The observed irregularity in the rates at 600 and 650°C was attributed to the crack deviation from RR1000 to IN718, as discussed elsewhere (Daus *et al.*, 2007). Moreover, the increase in test temperature was also associated with the dominance of intergranular fracture, compared with fully transgranular failure for the test performed at 500°C. The transition temperature (~600°C) between the transgranular and intergranular fracture supported the suggestion that an oxidation damage mechanism exists in Ni-based superalloys within this temperature range (Pint *et al.*, 2006). To identify the causes for the poor FCP at 650°C, Li *et al.* further investigated the influence

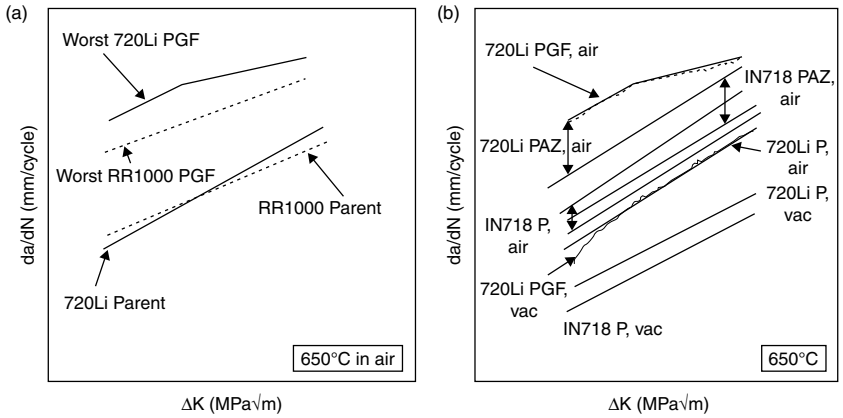

2.25 FCP in Ni-based superalloy inertia PWHT welds (Li *et al.*, 2007), showing the influence of (a) the parent material (IN718/RR1000 or 720Li welds), (b) the crack location (IN718–720Li).

of the starting parent metal on the FCP rate, as well as the influence of the sample location with respect to the weld. When testing welds of alloys of similar γ' fraction (RR1000 and U720Li), it was found that the worst FCP condition in the U720Li weld half, corresponding to the primary γ'-free zone (PGF), had a faster FCP rate compared with the similar condition in RR1000 weld (Fig. 2.25a). Moreover, the FCP rates were generally lower when tested in vacuum, with the highest rates occurring in the PGF zone, followed by the TMAZ (Fig. 2.25b).

2.4.2 Steels

Microhardness development

Depending on the type of the alloy, the microhardness development in steel IFWs showed several trends. In a low-carbon steel solid inertia friction weld, the hardness was generally highest at the weld centre, and decreased until it reached the base-metal hardness (Wang and Lin, 1974) (Fig. 2.26a). The hardness decreases from the centre of the weld interface outwards owing to the concavity of the weld region. In mild-steel tubular welds, the hardness was also high at the weld centre, yet it sharply decreased beyond the weld line within the HAZ, prior to increasing again as the base metal was approached (Fig. 2.26b).

In dissimilar steel inertia friction welds (e.g. SCMV-AerMet100 (Moat *et al.*, 2008; Robotham *et al.*, 2005)), the joining process results in a more complex microhardness distribution (Fig. 2.27). In an SCMV-AerMet100 IFW the three typical distinct zones, TMAZ, HAZ and base material, were

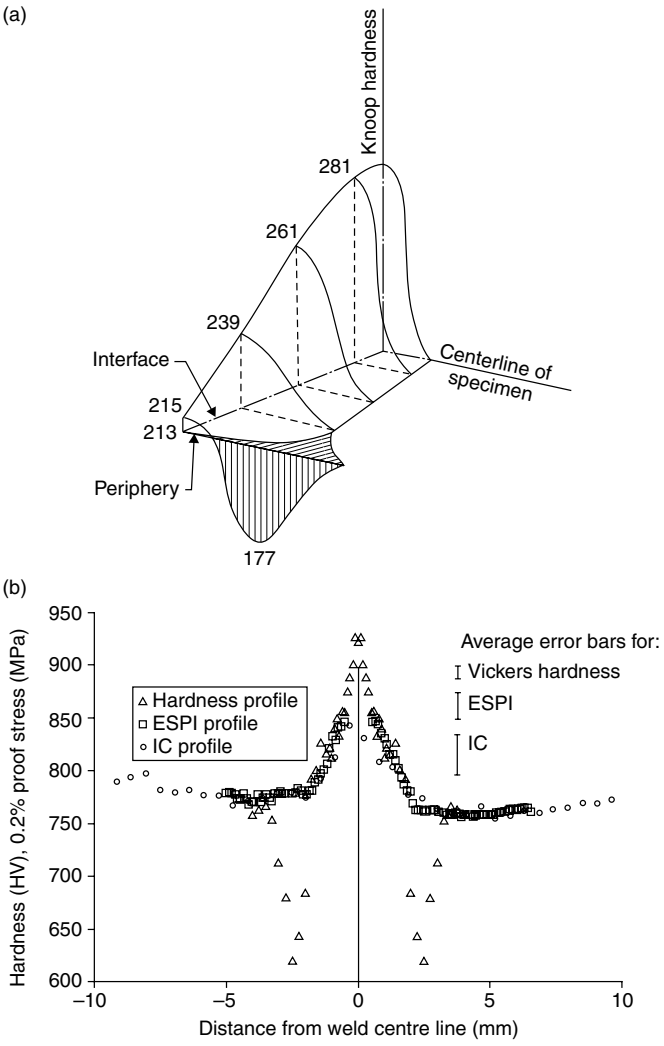

2.26 Microhardness development in steel inertia welds. (a) A quarter of a 3/8″ (9.5 mm) diameter solid low-carbon steel weld section, showing the local variations across the weld line and the depth (Wang and Lin, 1974), and (b) microhardness distribution in a mild steel inertia weld, alongside local mechanical properties (Fonseca *et al.*, 2004).

identified on each weld side. While in SCMV the hardness of the HAZ was lower than the base metal, in AerMet100 the hardness was actually higher than the base metal. Conversely, in the TMAZ of SCMV the hardness was higher than the base metal, while in AerMet100 it was lower. Following the PWHT, the extent of heterogeneity of the microhardness distribution

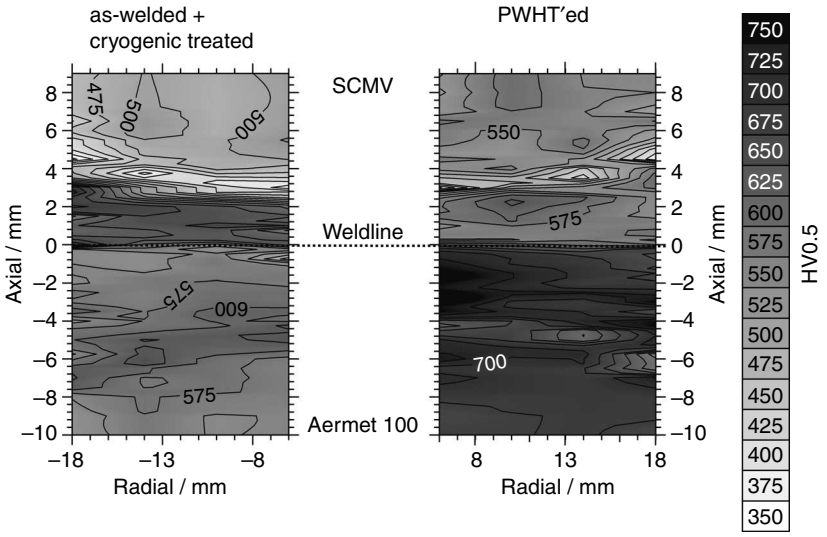

2.27 Microhardness distribution in the AW, and PWHT conditions for a SCMV-AerMet100 (Moat *et al.,* 2009).

decreased, with each side retaining a roughly uniform hardness distribution, except for a localised drop in hardness in the HAZ of both sides. These differences were attributed to the variation in the fractions of the phases present (e.g. martensite, austenite, ferrite and cementite) across the weld regions, depending on the alloy, cooling rates and temperatures experienced, as well as the heterogeneous plastic deformation at the TMAZ and aging of the M_2C carbides in the AerMet100 side.

2.4.3 Titanium alloys

Tensile properties

Early work by Nessler *et al.* (1971) studied the influence of IFW on the tensile, low-cycle fatigue (LCF) and reverse high-frequency bending properties of titanium-alloy inertia friction welds. It was shown that certain welding parameters (welding speed, forging pressure, surface roughness, joint squareness and concentricity) did not have a statistically significant influence on the mechanical properties. Nonetheless, on investigating the influence of the weld upset on the tensile properties, it became clear that both the tensile strength and ductility improved with the increase in upset (Fig. 2.28). The properties were generally reproducible in Ti-6Al-4V and Ti-6Al-2Sn-4Zr-2Mo IFWs once they were welded with the parameters that produced an upset of ~4 mm. Roder *et al.* (1999) also investigated the tensile strength of Ti-6246 IFWs at 20 and 300°C. The base-metal tensile strength

was achieved in all of the investigated welds, although the elongation was relatively lower than the base metal. The PWHT specimens generally failed in the base metal, while the AW specimens failed close to the weld centre.

Fatigue properties

Nessler *et al*. also investigated the LCF and high-cycle fatigue (HCF) properties of titanium inertia friction welds (Nessler *et al*., 1971). As shown in Fig. 2.29a, the Sonntag LCF shows that the majority of the PWHT welds displayed a superior behaviour than the base metal and the AW conditions.

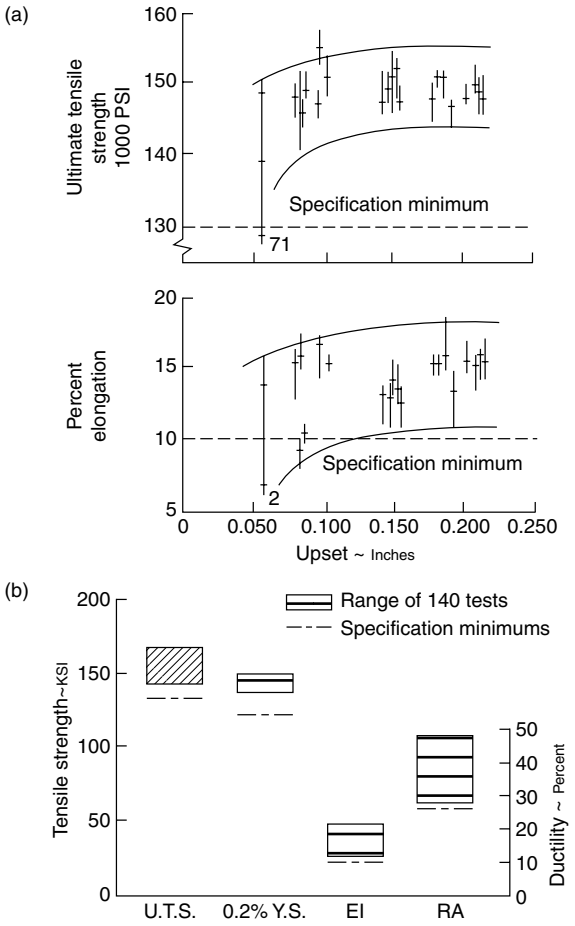

2.28 Tensile properties of titanium inertia welds. (a) Influence of the upset on the strength and elongation in Ti-6Al-4V welds and (b) reproducibility of Ti-6A-2Sn-4Zr-2Mo IWs (Nessler *et al.,* 1971).

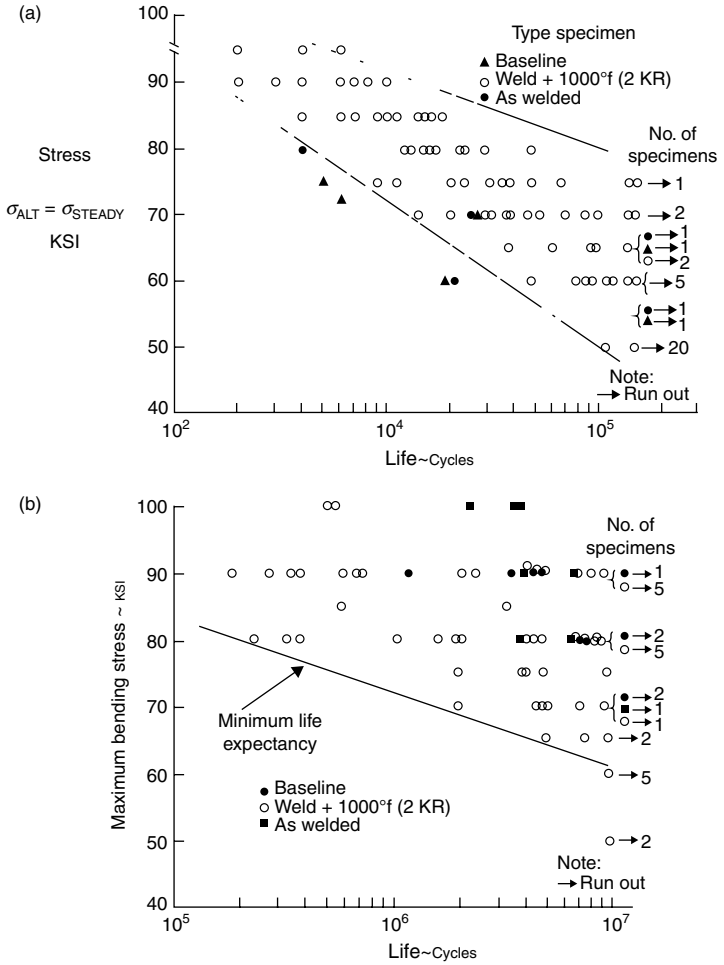

2.29 Fatigue properties of Ti-6Al-2Sn-4Zr-2Mo IWs. (a) Sonntag LCF and (b) reverse-bending high-frequency fatigue strength (Nessler *et al.,* 1971).

Similarly, the HCF tests (Fig. 2.29b) also show acceptable properties that occasionally surpass the base metal, with the failure occurring in the base metal. Other LCF investigations for Ti-6Al-2Sn-4Zr-6Mo (Roder *et al.*, 1999) and Ti-17 (Barussaud and Prieur, 1996) echo the findings of this study. It was found that even at relatively high temperatures (~300–400°C), the welds of Ti-17 and Ti-6242S have LCF and HCF properties that are comparable to the properties of the base metals of these alloys.

2.5 Residual stress development

Within the past decade, neutron and synchrotron X-ray diffraction have been extensively used to characterise the residual stress development in inertia friction welds owing to its capability of obtaining in-depth measurements, as opposed to hole drilling, which is only capable of performing surface measurements. Residual stress characterisation by diffraction involves measuring the change in the lattice parameters or interplanar spacing by measuring peak shift, and comparing it to the unaffected metal. The strains are then calculated using:

$$\varepsilon = \frac{d - d_0}{d_0} = \frac{a - a_0}{a_0} \qquad [2.13]$$

where d and a are the d-spacing and the lattice parameter, respectively, with the subscript '0' indicating the strain-free values. Following the measurement and calculation of the strain in all three directions (axial, radial and hoop), a stress component can be calculated using:

$$\sigma_{\text{Hoop}} = \frac{E}{(1+\upsilon)(1-2\upsilon)}\left[(1-\upsilon)\varepsilon_{\text{Hoop}} + \upsilon\left(\varepsilon_{\text{Radial}} + \varepsilon_{\text{Axial}}\right)\right] \qquad [2.14]$$

When undertaking such measurements great care has to be taken when determining the strain-free value d_0. Microstructural changes across the weld mean that the chemical compositions of the phases present in a multiphase engineering alloy have changed too. Consequently, d_0 is unlikely to be constant across the weld region requiring separate measurements of the d_0 variation or using stress-balance conditions (Preuss *et al.*, 2002b). Further details on residual stress characterisation and d_0 correction can be found elsewhere (Withers, 2001, Withers and Bhadeshia, 2001a, 2001b; Withers *et al.*, 2007).

Studies on the residual stress characterisation in tubular Ni-based superalloy inertia friction welds generally agree that the highest stresses in the weld occur in the hoop direction (Fig. 2.11), being tensile at the weld centre especially close to the inner diameter, and being limited by the yield strength of the alloy (Preuss *et al.*, 2006). In the axial direction, a lower stress intensity than in the hoop direction was measured but generated a bending moment. This bending moment was attributed to either the difference in temperature between the outer and inner diameters (Wang *et al.*, 2004), a tourniquet effect from the hoop stress owing to its cross thickness variation (Preuss *et al.*, 2006) or the influence of the clamping forces of the tooling (Fig. 2.30) (Pang *et al.*, 2003). It was also suggested that the influence of the tooling on the residual stress development could possibly be larger than the effect of the process parameters. Finally, minimal stresses occurred in the radial direction of these IFWs, which had a wall thickness of 8–11 mm.

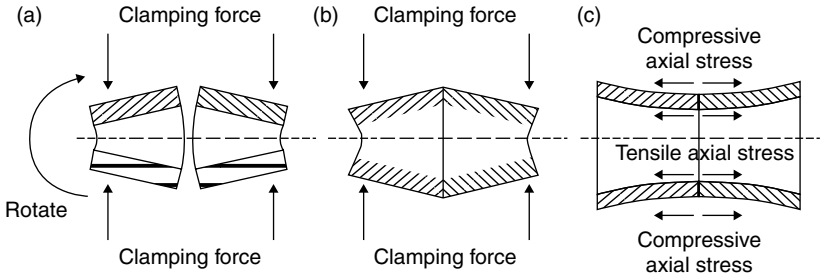

2.30 A schematic illustration for the development of the bending stresses in the axial direction. (a) Clamping leads to bending of the tube sections (exaggerated) prior to welding, (b) clamping is still applied during welding, and (c) upon the removal of the clamping forces, the ends are released, resulting in the formation of the axial stresses (Pang *et al.*, 2003).

Although different Ni-based superalloys generally have roughly similar spatial stress distribution and relative stress levels, differences in the magnitude of the stresses are normally found that are caused by the nature of the alloy microstructure and chemistry. Preuss *et al.* compared the residual stress development in RR1000, IN718, and U720Li (Fig. 2.31). The three welds had low radial stresses (±100 MPa), while the axial stresses all showed the before-mentioned bending profile with the maximum tensile and compressive stresses being ±350 MPa, ±450 MPa, and ±600 MPa in IN718, U720Li and RR1000, respectively. In the hoop direction, maximum tensile stresses of 700 MPa, 1000 MPa, and 1500 MPa were calculated in IN718, U720Li and RR1000, respectively. By calculating an equivalent stress using Von Mises equation, it was found that the equivalent stress in RR1000 weld centre exceeded the yield stress, suggesting that the stresses close to the weld line are limited by the local yield stress. In IN718 and U720Li, the weld stresses were generally lower than the yield stress (~0.8 σ_{ys}). This difference in the magnitude of stresses was attributed to the relatively poor short-term creep properties in IN718 and U720Li, allowing the misfit strains in these alloys to be reduced more during cooling than in RR1000. Upon performing PWHT, the major part of the stresses observed gets annihilated, although the hoop stresses remain generally high (~300–500 MPa) (Preuss *et al.*, 2006), while the axial and radial stresses decrease to ~±100 MPa (the experimental error in these measurements is ±60 MPa).

In contrast, residual stress characterisation studies of inertia friction welds produced of other materials (e.g. steels, titanium and aluminium alloys) are very limited, with a single report only available on dissimilar SCMV-AerMet100 steel welds (Moat *et al.*, 2009; Section 11.3.2). Ferritic steels differ from Ni-based superalloys in that IFW results in a phase

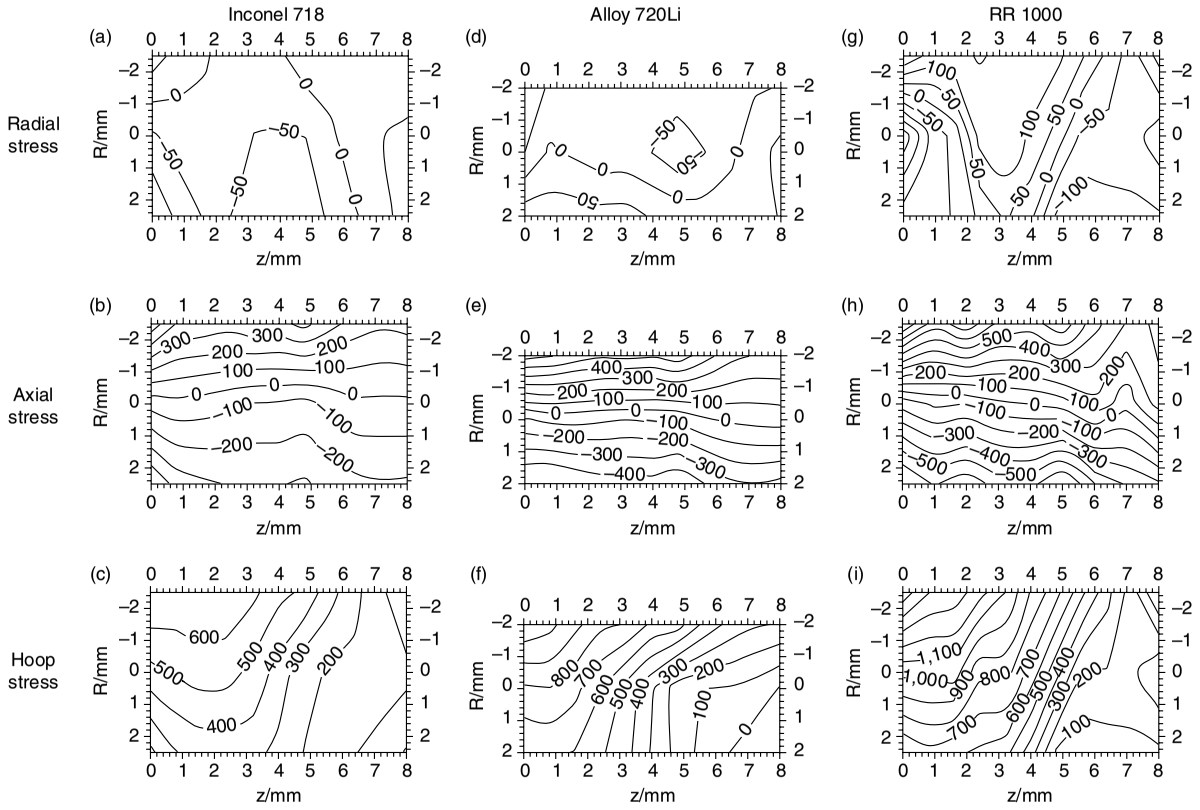

2.31 Residual stress contours in IN718 (a–c), U720Li (d–f) and RR1000 (g–i) (Preuss *et al.*, 2006).

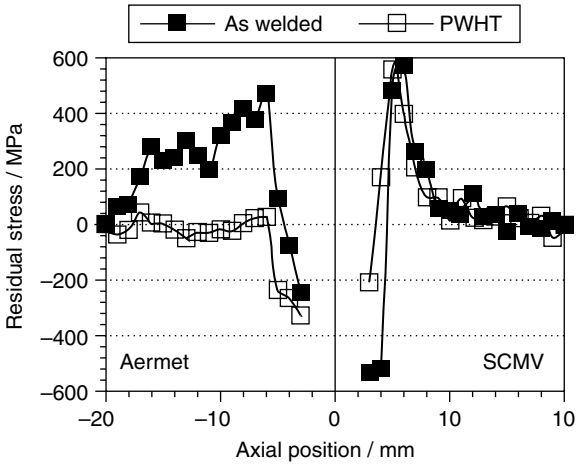

2.32 AW and PWHT hoop residual stress distribution in SCMV-AerMet100 (Moat *et al.,* 2009).

transformation during heating (ferrite to austentite), followed by the martensitic or bainitic phase transformation upon rapid cooling depending on the cooling rate and is affected by the wall thickness. As the formation of martensite is associated with a volume increase, this alters the stresses to become compressive near the weld line instead of the typical tensile stresses observed in this region. This can be viewed in the SCMV-AerMet100 hoop stress (Fig. 2.32), where the weld region (±2 mm) was predominantly compressive, as opposed to the Ni-based superalloys, which was tensile. Small stresses (100–300 MPa) were observed in both the radial and axial directions. Following PWHT, the stresses in AerMet100 generally dropped to acceptable levels, while almost no change was observed in the SCMV. These differences are because of the nature of the selected PWHT, and the differences between the two alloys in their thermal stability.

2.6 Future trends

Considering that IFW has been around for over half a century, it is clear that it can be classified as a mature technique, especially with respect to IFW of Ni-based superalloy aero engine parts. Nonetheless, there is a need for more extensive studies on IFW of steels, titanium and aluminium alloys owing to their potential applications in the aerospace industry. By browsing through the recent patents that are associated with IFW, several trends can be identified as potential future applications. There is an interest in using IFW to weld cylindrical components to thin non-cylindrical components, and dissimilar materials. The PWHT processes in several alloy inertia friction welds seem

to be a concern, as it is crucial to use a PWHT that results in the retention of the mechanical properties, especially the fatigue-resistance properties. Several patents also suggested new applications, including aircraft actuator pistons, gas turbine parts and crankshafts.

2.7 Source of further information and advice

For further information on IFW, especially machines and products, the reader is directed to the following web sites:

- Interface Welding: http://www.interfacewelding.com/
- Manufacturing Technology, Inc. : http://www.mtiwelding.com
- MTU Aeroengines: http://www.mtu.de/en/technologies/manufacturing_processes/inertia_friction_welding/index.html
- Swanson Industries: http://www.swansonindustries.com/inertiawelding.php
- The Welding Institute (TWI Ltd.): http://www.twi.co.uk
- Thompson Friction Welding: http://www.thompson-friction-welding.co.uk/

2.8 References

Adam, P. (1982) 'Material response during inertia welding of superalloys'. *Zeitschrift fuer Werkstofftechnik*, **13**, 258–262.

Anon (1979) 'Inertia welding: simple in principle and application'. *Welding and Metal Fabrication*, **10**, 585–589.

Baeslack III, W. A., Phillips, D., English, C. and Woodfield, A. P. (1991) 'Inertia-friction welding of an advanced rapidly solidified titanium alloy'. *Journal of Materials Science Letters*, **10**, 1401–1408.

Barussaud, A. and Prieur, A. (1996) 'Structure and properties of inertia welded assemblies of Ti-based alloy disks'. *Titanium '95 – Science and technology; the 8th World Conference on Titanium*. Birmingham, United Kingdom.

Benn, B. (2000) 'Inertia welding' (unpublished).

Bennett, C. J., Hyde, T. H. and Williams, E. J. (2007) 'Modelling and simulation of the inertia friction welding of shafts'. *Proceedings of the Institution of Mechanical Engineers*, *Part L*: *Journal of Materials*: *Design and Applications*, **221**, 275–284.

Cheng, C. J. (1962) 'Transient temperature distribution during friction welding of two similar materials in tubular form'. *Welding Journal*, **41**, 542S–550S.

Cheng, C. J. (1963) 'Transient temperature distribution during friction welding of two dissimilar materials in tubular form'. *Welding Journal*, **42**, 233S–240S.

Chudikov, A. I. (1956) 'Friction Welding'. *Russian Patent*, **RU106270**.

D'Alvise, L., Massoni, E. and Walloe, S. J. (2002) 'Finite element modelling of the inertia friction welding process between dissimilar materials'. *Journal of Materials Processing Technology*, **125–126**, 387–391.

Daus, F., Li, H. Y., Baxter, G., Bray, S. and Bowen, P. (2007) 'Mechanical and microstructural assessments of RRiooo to IN718 inertia welds – effects of welding parameters'. *Materials Science and Technology*, **23**, 1424–1432.